Simulations Of Galaxy Clusters With And Without Winds I. The Structure Of Clusters

Christopher A. Metzler¹

NASA/Fermilab Astrophysics Group, Fermi National Accelerator Laboratory, Box 500, Batavia, IL 60510-0500 USA

August E. Evrard²

Department of Physics, University of Michigan, Ann Arbor, MI 48109-1120 USA and Institut d'Astrophysique, 98bis Blvd. Arago, F75014 Paris, France

ABSTRACT

We use gas dynamic simulations to explore the effects of galactic winds on the structure of the intracluster medium (ICM) in X-ray clusters. Two ensembles of 18 realizations, spanning a decade in temperature T, are evolved with and without galactic winds in an underlying standard CDM cosmology with $\Omega = 1$ and $\Omega_b = 0.1$. Galaxies are identified as peaks in the initial, linear density field, and are assumed to lose half their initial mass over a Hubble time in winds with effective temperature $T_{wind} = 8$ keV.

The extra wind energy raises the entropy of the gas above the level generated by gravitationally induced shocks. This leads to substantially lower central densities in the ensemble with winds compared to the ensemble lacking winds. The magnitude of this effect increases with decreasing mass or virial temperature, and results in a trend of shallower gas profiles at lower temperatures, consistent with observations. In contrast, we find the final temperature of the gas is relatively unaffected; a similar mass—temperature relation results with or without winds. The input wind energy, which is comparable to the thermal energy in low temperature systems, is effectively consumed as work to lift the gas in the dark matter dominated potential.

¹metzler@denali.fnal.gov

²evrard@umich.edu

Radially averaged temperature profiles of models with winds are slightly steeper than those without. The extended nature of the ICM with winds can lead to underestimates of the global baryon fraction; we calibrate the amplitude of this effect at density contrasts $\delta_c = 170$ and 500. These features should be generic to all wind models.

The structure of the dark matter density profiles is consistent with the form proposed by Navarro, Frenk & White, and we find evidence for higher central concentrations in lower mass systems, consistent with previous, purely N-body studies. The galaxy distribution in the ensemble with winds is cooler and more centrally concentrated than either the dark matter or gas. A mild, but persistent, velocity bias exists, with ensemble average value $\sigma_{gal} \simeq 0.84\sigma_{DM}$.

The steep nature of the galaxy spatial distribution, combined with ejection of metal enriched material over a Hubble time, produces a strong, negative radial gradient in metallicity within the ICM. Core radii remain unresolved, even in the models with winds. These features are sensitive to the assumed wind history of the galaxies.

Subject headings: Galaxies-clusters, cosmology-theory

1. Introduction

A variety of mature observational techniques are now in use studying galaxy clusters. Through optical studies of cluster galaxies, analyses of weak gravitational lensing distortions of the background galaxy field, observations of radio sources within and behind clusters, and X—ray images and spectra of the intracluster medium (ICM), we now have a wealth of data to compare to models of clusters drawn from analytic treatment and numerical simulation.

The paradigm for cluster formation and evolution that has emerged from such modeling is one in which clusters form through gravitational collapse of an overdense region (Gunn & Gott 1972; Bertschinger 1985). While analytical descriptions typically assume spherical symmetry, cluster observations and N-body simulations of hierarchical clustering from initially Gaussian, random density fields show that the collapse process is generally irregular, involving mergers of protoclusters flowing along large—scale filaments, along with accretion of smaller satellite systems and weakly clustered material.

It is commonly held that rich clusters formed at recent epochs. Nevertheless, since the relaxation timescales for clusters are significantly less than a Hubble time, the standard model for describing the distribution of matter within clusters is one based on hydrostatic equilibrium. Early one–dimensional collapse simulations by Perrenod (1978) supported this assumption, later confirmed in three–dimensions by Evrard (1990a,b). The isothermal β –model (Cavaliere & Fusco–Femiano 1976, 1978; Sarazin & Bahcall, 1977) makes further simplifying assumptions of an isothermal ICM temperature and spherical symmetry of an assumed, dominant collisionless potential, now taken to be generated by dark matter. Each component follows a density profile of the form

$$\rho(r) = \rho_0 \left[1 + \left(\frac{r}{r_c} \right)^2 \right]^{-3\alpha/2} \tag{1}$$

where r_c is the core radius within which the density profile relaxes to a constant, central value ρ_0 . In this model, the outer profile slopes of the gas and dark matter, measured by their respective values of α , provide information on the relative temperatures of the two components. The parameter

$$\beta \equiv \frac{\sigma^2}{\left(\frac{kT}{\mu m_p}\right)}.$$
 (2)

from which the model takes its name, is the ratio of specific energy in dark matter, measured by the one-dimensional velocity dispersion σ , to that in gas, measured by its temperature T and mean molecular weight μ , with k Boltzmann's constant and m_p the proton mass. Since the ICM mass dominates the galaxy mass in rich clusters such as Coma

(Briel, Henry & Bohringer 1992; White et al. 1993), it is reasonable to assume that the ICM plasma originates in primordial gas leftover from galaxy formation. In this case, the gas and galaxies cluster hierarchically within the same potential wells, so it is similarly reasonable to expect that the specific energies of the two components will be nearly equal, $\beta \simeq 1$. (A refined discussion of this point is provided in the Appendix.)

However, there is evidence that the history of the intracluster medium is more complicated. In particular, the presence in the ICM of iron and other elements produced by stars, at abundances near solar, necessitates significant interaction between galaxies and the hot intracluster plasma. Mechanisms for this metal enrichment process include feedback from a very early stellar population such as Population III stars (Carr, Bond & Arnett 1984), ram pressure stripping by the ICM of the interstellar medium from galaxies (Gunn & Gott 1972; Biermann 1978; Takeda, Nulsen, & Fabian 1984; Gaetz, Salpeter, & Shaviv 1987), and ejection of hot enriched gas from galaxies via winds (Yahil & Ostriker 1973; Larson & Dinerstein 1975). How might we discriminate between these?

First of all, a key question with respect to the dynamics of the ICM plasma is whether significant energy deposition accompanied the enrichment process. "Passive" mechanisms, such as primordial enrichment or ram pressure stripping, do not add considerable energy to the ICM. Galactic winds, on the other hand, represent an "active" mechanism which deposits both energy and metal enriched material into the ICM. Meanwhile, there is some evidence implying cluster gas has a greater specific energy than cluster galaxies, or $\beta < 1$ (cf. Edge & Stewart 1991), a result consistent with additional, non-gravitational energy input into the ICM. Also, several studies of the relation between the galaxy velocity dispersion and ICM X-ray temperatures in clusters suggest that β varies with the depth of the potential well (Edge & Stewart 1991; Lubin & Bahcall 1993; Bird, Mushotzky, & Metzler 1995; Girardi et al. 1995). To be fair, cluster velocity dispersions and X-ray temperatures are difficult to compare in an unbiased manner, since the quantities are prone to different types of systematic errors and are typically not measured within the same region of a cluster (Metzler 1997). However, if robust, such a result may be expected from wind models. Since the specific energy of an individual galactic wind should not depend upon the host cluster whereas the specific thermal energy supplied by gravitational collapse does depend on cluster mass, winds should affect more strongly the ICM of clusters with small velocity dispersions. This may introduce a dependence of the ratio of specific energies with temperature in the manner described above.

Another possible discriminant between enrichment mechanisms lies in the distribution of metals in the intracluster medium. However, it is difficult to infer analytically the type of abundance gradient expected from each of these three mechanisms. Simulations of cluster evolution incorporating enrichment can clarify this, and provide an expectation to compare to observations of abundance gradients now becoming available (e.g. Tamura et al. 1996; Xu et al. 1997; Ikebe et al. 1997).

We present here results from an ensemble of simulations which include the effects of galactic winds in a self-consistent, three-dimensional fashion. A unique feature of these is the ability to trace the structure of galaxies and metal-enriched gas in the ICM. This work expands the examination of a single, Coma-like cluster presented in an earlier paper (Metzler & Evrard 1994, hereafter Paper I). Since galactic wind models themselves are uncertain, we take a heuristic approach and employ a simple, and in some ways extreme, model for galactic winds in an attempt to explore the upper envelope within which realistic models should lie. We examine an ensemble of eighteen cluster realizations, spanning a factor of 50 in cluster mass, drawn from a standard cold dark matter cosmogony. Each initial realization is evolved twice, with one run incorporating and the other ignoring galaxies and their ejecta. This paper focuses on the three-dimensional structure of the present epoch population; a subsequent paper will examine the effect of feedback on X-ray observations.

In Section 2, we elaborate on the numerical techniques used in this work, as well as the general properties of the two cluster ensembles used. Section 3 provides a look at the structure of the collisionless components (dark matter and galaxies) in these simulations. The structure and metal distribution of the intracluster medium are examined in Section 4. A revised model of the ICM, based on the halo model of Navarro, Frenk & White (1996, hereafter NFW2), is considered in Section 5. The relative structures of the various cluster components are compared in Section 6; also included there are some comments about implications for estimates of the cluster baryon fraction. Our results are summarized in Section 7.

2. Method

2.1. Initial Conditions

The simulations and their initial conditions use as their basis the standard biased cold dark matter (CDM) scenario (Blumenthal et al. 1984; Davis et al. 1985): $\Omega = 1$; baryonic fraction $\Omega_b = 0.1$; Hubble constant h = 0.5; and power–spectrum normalization $\sigma_8 = 0.59$. These parameters are used throughout this work when scaling to physical units. The path–integral formalism of Bertschinger (1987) is used to generate initial density fields which are constrained, when smoothed with a Gaussian filter, to have a specified value at the

center of the simulated volume. For the simulations in this paper, we filter with a Gaussian of scale $R_f = 0.2L$ Mpc, where L is the length of the periodic volume, corresponding to a mass scale of $M_f = (2\pi)^{3/2} \rho_c R_f^3 = 5.6 \times 10^{14} (L/40 \text{ Mpc})^3 \text{ M}_{\odot}$ (Bardeen et al. 1986). Here $\rho_c = 3\text{H}_0^2/8\pi G$ is the critical density, also the mean background density of the models. The perturbation height at the center was constrained to a value $\delta_c = 2.0$ when filtered on scale M_f . For all of the simulations described in this paper, $32^3 = 32768$ particles are initially placed for each of the dark matter and gas fluids; the mass of an individual dark matter particle is related to the mass of a gas particle by $m_{DM} = 9m_{gas}$, reflecting their fractions of the total density. The primordial density field is used to generate a particle distribution at the starting redshift $z_i = 9$ using the Zel'dovich approximation, as described in Efstathiou et al. (1985).

Since in generating the constrained initial density field, we filter on a fixed fraction of the box length, we can simulate clusters spanning a range in mass simply by varying the box size. The mass per simulation particle is proportional to L^3 , but so is the filter mass scale. This causes the number of particles in the final collapsed object to be roughly comparable in all runs, so the fractional mass resolution in the various simulations presented here is equivalent. This avoids any systematics that might be introduced into correlations between cluster quantities (X-ray luminosity vs. mass, for example) if the resolution varied in a systematic way from low-mass to high-mass clusters.

2.2. Including Galaxies

The technique used for inserting galaxies in the simulation is described in detail in Paper I. We Gaussian-filter the initial conditions on the approximate scale of bright galaxies ($R_f = 0.5$ Mpc, corresponding to $M_f = (2\pi)^{3/2} \rho_c R_f^3 = 1.4 \times 10^{11} \mathrm{M}_{\odot}$) and locate peaks in the initial overdensity field on that scale above a fiducial threshold of 2.5σ , chosen to reproduce the observed number density of bright galaxies. We then return to the initial particle distribution and replace the gas particles associated with each peak with a composite "galaxy particle." We assume an effective collapse redshift of $z_c = 4.5$, corresponding to a linearly determined mean interior overdensity at the starting redshift z_i of

$$\delta_{gal} = 1.686 \frac{1+z_c}{1+z_i} = 0.933. \tag{3}$$

The gas particles within this mean interior overdensity are removed, and the mass of the resulting galaxy particle is set to the number of gas particles removed. The initial linear momentum of a galaxy particle is set by demanding conservation of linear momentum.

A valid concern with our method and results can be raised over our use of peaks to simulate galaxies. The most natural thing to do would be to allow the gas in the simulations to cool and form galaxies, and then allow those galaxies to provide the sources for the feedback into the intracluster medium. However, such an approach suffers from limitations in our ability to accurately model star formation, in both a physical and numerical sense. As we wish to perform many simulations to ensure adequate statistics when considering issues of cluster structure and evolution, we must economize computational resources spent on an individual run, and our approximate peak treatment to galaxy formation provides considerable numerical savings. The peak model has some physical basis in that there is known to be "crosstalk" from large to small scales during hierarchical clustering from Gaussian initial conditions in the non-linear regime which enhances the rate of small-scale structure formation for the power spectrum shape considered here (White et al. 1987; Juszkiewicz, Bouchet, & Colombi 1993). The model also has some phenomenological success in explaining the qualitative shape of galaxy luminosity functions (Evrard 1989) and the morphology-density relation in clusters (Evrard, Silk & Szalay 1990).

However, since the theory of Gaussian random fields (Bardeen et al. 1986) tells us that peaks on smaller scales are likely to be biased towards peaks on larger scales, and since our initial conditions are constrained to produce a high-peak on cluster scales at the center of the simulation volume, the initial galaxy distribution will be more centrally concentrated than the overall mass distribution. The thermal history and metal distribution of the ICM is certainly sensitive to the assumed galaxy formation model. To quantify this, several runs were performed with galaxies placed randomly in the volume, rather than at the locations of overdense peaks. By removing the peak correlations induced by the presence of the cluster, random placement resulted in a substantial reduction in the number of bright galaxies within the simulated clusters, even though the number density in the entire simulated volume was held fixed. The effect of feedback was reduced to the point that the ejection runs differed little from their non-ejection counterparts, and so we do not discuss these runs further in this paper. High resolution numerical experiments resolving galaxy formation within clusters will ultimately settle this question. The current best effort on this issue favors the peaks approach over random placement (Frenk et al. 1996).

2.3. Numerical Algorithm and the Wind Model

We use the N-body + hydrodynamical algorithm P3MSPH, which combines the well known particle-particle-mesh (P^3M) algorithm of Efstathiou & Eastwood (1981) with the Smoothed Particle Hydrodynamics (SPH) formalism of Gingold &

Monaghan (1977). The combined algorithm is described in Evrard (1988), and some of the post–simulation analysis procedures used are described in Evrard (1990b) and Paper I.

The simulation algorithm can follow collisionless dark matter and collisional baryonic gas; we have modified the simulation algorithm to also model galaxy particles of varying mass, and to allow the galaxies included to eject energetic, metal-enriched gas. The technique used is described in detail in Paper I. The galaxy mass fraction lost through winds is described by a time-dependent rate curve; specific energy and iron ejection rate curves are also assumed as input. For each galaxy, the wind rate curve is integrated until the amount of mass ejected equals the mass of a simulated gas particle. Energy and iron mass fraction are then assigned to that particle by integrating those curves over the same period. The process is then repeated for as long as the ejection rate curve is non-zero. Thermal energy, momentum, and iron mass are mixed approximately over the scale of one SPH smoothing length. The smoothing process, described in detail in Paper I, is based on conservation of mass, momentum and energy and a scenario in which wind ejecta is rapidly mixed into the surrounding ICM. For these simulations, we have assumed a wind model in which galaxies eject half their mass at a flat rate from a redshift of four to the present, with a wind luminosity for a galaxy with $10^{10} \rm M_{\odot}$ in baryons of $L_{wind} = 4 \times 10^{42} \rm \ erg\ s^{-1}$, and a total energy release of 1.5×10^{60} erg.

2.4. The Cluster Ensemble

To study systematic trends, it is necessary to examine an ensemble. To this end, we assemble 18 sets of initial conditions, and evolve them with and without galaxies and winds, for a total of 36 simulations. Five comoving box lengths are used. For comoving box lengths of 20, 25, and 30 Mpc, four sets of initial conditions each are used, while three each are run at 40 and 60 Mpc. A summary of general properties of the runs is shown is Table 1. As in Paper I, we refer to the ensemble of runs with galaxies and winds as the EJ, or ejection, ensemble, and the runs without galaxies as the 2F, or two-fluid, ensemble. When referring to individual runs in this paper, all run names begin with the comoving box length in megaparsecs and end with a suffix to differentiate between runs. We will indicate whether ejection is included as appropriate.

3. The Collisionless Components

3.1. Clusters Sizes and Characteristic Scales

In formation via graviational instability, one expects a characteristic length to emerge which divides the regions within which material is close to hydrostatic equilibrium and exterior to which matter is on its first infall or expanding (Gunn & Gott 1972; Rivolo & Yahil 1984; Bertschinger 1985). Because infall occurs on a gravitational timescale $t_{grav} \propto \rho^{-1/2}$, one expects this characteristic radius to occur at a fixed value of the mean enclosed density. Figure 1 shows the radial velocity profile at z=0.02 for the dark matter in four of the two-fluid simulations using mean interior density contrast as the abscissa, defined as $\delta_c = \rho(\langle r)/\rho_c$. These four were chosen because they have qualities worth describing in more detail; the remaining clusters have similar structure. All show a velocity profile characteristic of gravitational collapse in an expanding world model. Spherical clusters would have a zero velocity surface at a density contrast of ~ 5.5 (Peebles 1980). As shown by the outer dashed line, this overdensity does an excellent job of marking the turnaround radius. In run 20e, the velocity magnitude in the region of infall is somewhat small, and the infall occurs over a narrow range of overdensities. This simulation forms three small clusters of approximate mass ratios 2:2:1, and the two largest objects are near each other, causing the infall region in each to be weak due to interference from the other cluster.

There is not an obviously sharp transition marking the virialized region. Some simulated clusters, such as the 20b and 40a runs shown, have a reasonably quiescent region interior to a region of strong infall. For these clusters, the rough prediction of the spherical model — the inner dashed line at an overdensity of 170 — provides a good approximation to the outer boundary of the virialized region. Other objects, however, have a complicated velocity structure within this overdensity. In particular, the most massive clusters exhibit infall extending into much larger overdensities. Massive systems form later, and these clusters are still experiencing strong infall and are not relaxed. The three worst offenders — runs 40c (shown), 60c, and 60d — experience strong mergers and asymmetric accretion after a redshift of 0.5.

Nonetheless, since no other characteristic virial overdensity emerges from the data, we use the radius with a mean interior overdensity of 170, hereafter called r_{170} , as a fiducial virial radius in the analysis below. Cluster properties such as density and temperature will then be profiled against the scaled radius $x = r/r_{170}$. For convenience, the relation between r_{170} and total cluster mass M_{170} is

$$r_{170} = 1.72 \left(\frac{M_{170}}{10^{15} h^{-1} M_{\odot}}\right)^{1/3} h^{-1} \text{ Mpc.}$$
 (4)

If clusters are very nearly self-similar over the range in mass probed here, then the choice

of another overdensity value for the virial scale merely amounts to relabelling the radial coordinate of our profiles. Much of the literature follows the example of Navarro, Frenk & White (1995, hereafter NFW1), who employ an overdensity of 200. However, Evrard, Metzler & Navarro (1996, hereafter EMN) demonstrate that a density contrast of 500 is a more conservative choice for the hydrostatic boundary of clusters, in the sense that the mass weighted radial Mach number has smaller variance and an ensemble mean more consistent with zero within r_{500} than r_{200} . For power–law density profiles near r^{-2} , r_{200} and r_{170} differ by about 8%.

The mass, mean dark matter velocity dispersion, and intracluster medium temperature within a radius r_{170} for the members of the two-fluid ensemble are shown in Table 2. Although the simulations span a factor of 27 in volume, the resulting clusters span a factor of nearly 50 in mass. This difference is due to the fact that in two of the smallest volume runs, two clusters of comparable mass form and have not merged by the end of the simulation. For the analyses here, the larger of the two clusters in each simulation was chosen. In Table 3, we give information for the ejection ensemble, including the global fraction of the initial gas mass remaining in the volume after insertion of galaxies (f_{gas}), the number of galaxies in the simulation, the number within r_{170} of the present epoch cluster, and the mean temperature of ICM within that radius. Gas and galaxy fractions within the clusters are discussed in §VI. The masses and dark matter velocity dispersions for the ejection ensemble are very similar to their two-fluid counterparts, so we do not quote them here.

3.2. Dark Matter Density Profiles

We now consider the dark matter distribution of the simulated clusters. The dark matter structure in the runs with galaxies and ejection is nearly identical to their two-fluid counterparts, so we present results from only the 2F set in this and the following section.

Figure 2 shows the dark matter density profiles for the eighteen clusters in our ensemble, taken at z=0.02. These profiles were constructed by defining radial bins containing 200 particles each, then measuring the volume of the bin to arrive at the density. The shapes of the profiles look remarkably similar. In Figure 3a, the profiles have been rescaled; we plot the local density contrast ρ/ρ_c , versus scaled radius $x=r/r_{170}$. There is some difference in central overdensity between models, but at larger radii (smaller overdensities), this dispersion tightens. Vertical lines in both figures denote the values of the gravitational softening parameter ϵ for each individual run at this epoch. The agreement among the density profiles of the ensemble reinforces previous findings of a characteristic

density profile for halos formed via hierarchical clustering. The self–similarity displayed in this figure confirms the choice of r_{170} as a scale radius, although choices of overdensity near this value would work equally well.

Motivated by the self–similar appearance in Figure 3a, we construct a mean density profile for the two–fluid runs by averaging the values of the density derived from each individual cluster in radial bins evenly spaced in $\log(x)$. The result, along with comparison to various functional forms, is shown in Figure 3b. Each of these functions has at least two adjustable parameters — an amplitude, and either a scale length or an exponent. However, it is important to note that one parameter is constrained by the required mean overdensity interior to r_{170} . In fitting to these functions, only data within r_{170} are used.

We first consider a fitting function of the form introduced by NFW1

$$\frac{\rho(x)}{\rho_c} = \Delta \left(\frac{x}{\lambda}\right)^{-1} \left[1 + \left(\frac{x}{\lambda}\right)\right]^{-2} \tag{5}$$

where, as before, $x = r/r_{170}$, the scaled radius of Figure 3. This profile approximates an r^{-1} power law at small radii, and an r^{-3} power law at large radii. The characteristic scaled radius λ , or physical radius λr_{170} , is the radius at which the logarithmic slope of the density profile is -2; Δ is four times the local overdensity at that radius. Since we will apply this functional form to the entire density profile, our integral constraint requires that

$$\Delta = \frac{170}{3\lambda^3 \left[\ln \left(1 + \frac{1}{\lambda} \right) - \frac{1}{1+\lambda} \right]}.$$
 (6)

A single member of this class of functions with fixed values $\lambda=0.2$ and $\Delta=7500$ was introduced by NFW1, and shown to model well the inner profiles of their simulated CDM clusters. Subsequent work (NFW2; Metzler 1995; Cole & Lacey 1996; Tormen, Bouchet & White 1997) generalized this profile to allow λ to be a free parameter. When applied to our mean profile, this form provides an excellent fit, with a best fit $\lambda\simeq0.154\pm0.008$ (implying $\Delta\simeq13600$). Our normalization looks much larger than the original NFW1 result but, as explained below, the discrepancy is due to differences in the samples employed in the studies.

If we apply this form to two subsets of the ensemble, one comprised of the six highest–mass runs and one comprised of the eight lowest–mass runs, we find that the mean profiles are significantly different, with the high mass ensemble requiring a higher value of λ (0.176 ± 0.010) than the low mass ensemble (0.145 ± 0.005). A small value for λ corresponds to a steeper inner density profile; low mass CDM halos are more centrally concentrated than high mass halos. The difference in density structure between high and low mass objects reflects the formation epochs of different objects. In hierarchical clustering cosmogonies

such as CDM, lower mass objects form earlier, when the background density is higher, so their mass is expected to be more centrally concentrated. This effect is expressed clearly by NFW2, who examine halos spanning four decades in mass. It is this mass dependence which explains the difference between our best fit parameters and the original NFW1 values. Our fits are, in fact, in good agreement with the standard CDM case considered in NFW2 (their Figure 5).

Contrast the seeming success of this model with the standard β -model profile, Equation 1, which provides a three-parameter fitting function as

$$\frac{\rho(x)}{\rho_c} = \Delta_0 \left[1 + \left(\frac{x}{x_c} \right)^2 \right]^{-3\alpha_{DM}/2}.$$
 (7)

This functional form implies a central, constant density core, characterized by the core radius $r_c = x_c r_{170}$ and central density $\Delta_0 \rho_c$. Using this expression, we find a best-fit core radius of $x_c = 0.053$, slightly under twice the mean softening scale (see Figure 3). At such a radius, the deviation of the softened force from a normal Newtonian force law is significant, so we cannot claim to resolve such scales in the mean profile. Fits of this function to the density profiles of individual clusters produce resolvable core radii only in systems with recent or in-progress merger activity. We therefore cannot claim to resolve any core in our simulated clusters' density profiles, in agreement with numerous previous studies. The implied large-radius logarithmic slope for the mean profile is $-3\alpha_{DM} = -2.48$.

The simplest description of the density profile is that of a power law, $\rho(x) \propto x^{-\alpha}$. The curvature in the density profiles evident in Figure 2 implies that a power law is inappropriate over the entire range of resolved structure, and formal fits verify its inadequacy. It is worth noting, however, that while the curvature is clearly present, it is not extreme. The local logarithmic slope of the density profile lies between -1.5 and -2.5 over the entire resolved range, lending support to analyses of cluster structure which assume isothermality. Considering only radii with a local overdensity in the range $100 \le \rho/\rho_c \le 3000$, a power law with $\alpha = 2.39 \pm 0.08$ provides an excellent fit to the mean profile. This result is consistent with the value 2.33 ± 0.04 found in the $\Omega = 1$, n = -1 model of Crone, Evrard & Richstone (1994). At smaller radii, the profile is more shallow; a fit between local density constrasts of 10^5 and 5000 yields $\alpha = 1.56$. The spatial and mass resolution of the experiments is not sufficient to demonstrate convergence to this, or any other, value of the logarithmic slope of the dark matter density as $x \to 0$.

Parameters extracted from fits to the dark matter profiles are summarized in Table 4. There are several important points to summarize. First, the clusters have a characteristic density profile consistent with those found in previous studies. The logarithmic slope of the profile is typically shallower than -2 at small radii, and steeper at large radii; the division

between these two regions occurs between $0.1\text{--}0.2~r_{170}$, depending upon the mass of the cluster. For clusters with emission weighted X-ray temperatures of 7 keV or so, this should correspond to radii of about 350–700 kpc at the present. The degree of central concentration is mass-dependent, with less massive clusters being more centrally concentrated. The outer portions of cluster density profiles are well-approximated by power-laws and demontrate less sensitivity to mass. There is no evidence that CDM clusters have or even approach constant density cores. The behavior of the density profile in the very central regions of clusters remains uncertain; recent high resolution simulations exhibit central profiles steeper than that prediced by the NFW form, Equation (5) (Moore et al. 1997).

3.3. Dark Matter Velocity Dispersion Profiles

The top half of Figure 4 shows the dark matter velocity dispersion profile for the eighteen members of the two-fluid ensemble. The profiles have been rescaled — the radial coordinate by r_{170} for each cluster, and the velocity dispersion by the quantity σ_{170} , defined as

$$\sigma_{170} = \left(\frac{GM_{170}}{2r_{170}}\right)^{1/2},\tag{8}$$

where M_{170} is the mass within r_{170} . Most of these profiles have a common shape, rising from the center of the cluster and then falling again towards the virial radius, but recent merger activity causes deviations from this profile for some systems. As noted earlier, the typical dark matter density profile for the ensemble is shallower than r^{-2} at small radii, and steeper at larger radii, corresponding to the velocity dispersion profiles seen. The radius at which the velocity dispersion is a maximum will lie somewhat beyond the break radius at which the density profile has a local logarithmic slope of -2. For the NFW profile, if we assume the velocity dispersion to vary weakly with radius (true for the simulated clusters), and that velocity anisotropy is unimportant, then the location of the velocity dispersion maximum can be calculated to lie at $x_{max} \simeq 1.16\lambda$; the mean profile would then predict the maximum of the velocity dispersion at $x_{max} \simeq 0.18$, very near where most of the curves originates from transients associated with mergers and/or the presence of long-lived orbital anisotropy in the velocity distribution.

The bottom half of the figure shows the velocity dispersion anisotropy parameter, $A(r) = 1 - \sigma_t^2/\sigma_r^2$, where σ_r and σ_t are the dispersions in the radial and transverse velocities respectively. The dark matter orbits are mostly radial over much of the profile for all of the members of the ensemble, reducing the kinetic support somewhat and steepening the dark matter density profile. At small radii, the dispersions converge towards isotropy,

although one run (60d) shows evidence for the irregular state noted in its radial velocity profile.

3.4. Galaxy Number Density Profiles

Representation of galaxies as a separate, collisionless component in the ejection ensemble allows us to investigate the kinematics of this visible population. We fit the distribution of galaxies in the simulated clusters to a β -model profile. Galaxy number density profiles are determined by constructing Lagrangian radial bins for each simulated cluster, holding five galaxies each, out to r_{170} . The central two bins of each profile are excluded from the fit, to minimize the effect of force softening on the results. This makes determination of central galaxy number density and core radius uncertain; but these parameters are of questionable value, since in real clusters their determination is prone to a variety of errors, particularly from the choice of cluster center. We can estimate the large-radius logarithmic slope of the galaxy number density profile, and address the question of whether the dark matter is more extended than the galaxy distribution. Finally, we consider only cluster profiles which have at least eight fitting bins after this exclusion, and thus at least five degrees of freedom. This requires at least 50 galaxies within r_{170} .

Figure 5 shows the galaxy number density profiles of the six largest clusters in the ensemble — the only six that fit the minimum criteria above. Also shown are best–fit β –model profiles. In five of the six cases, the large–radius slope of the galaxy number density profile $-3\alpha_{GAL}$ is steeper than that of the dark matter; the dark matter is more extended than the cluster galaxies. Although the number statistics here are poor, a comparison of cumulative masses using the entire ensemble, shown in §VI, clearly demonstrates that the galaxy population is, in the mean, more centrally concentrated than the dark matter.

3.5. Velocity Bias

Since our initial placement of galaxies is upon peaks in the density field, and since such peaks are expected to be spatially biased towards the peak on large mass scales associated with the cluster itself, the galaxies are expected to be somewhat more centrally concentrated than the dark matter. There are, however, physical mechanisms which can contribute to such concentration. Apart from the contribution of galaxies to the overall cluster potential well, the distribution of galaxies and dark matter will be affected to some degree by interactions between the two components (Barnes 1985; Evrard 1987; West &

Richstone 1988; Carlberg 1991; Carlberg & Dubinski 1991; Carlberg 1994). Given a CDM halo which is initially well—traced by the distribution of galaxies, dynamical friction will transfer energy from the galaxies to the dark matter, resulting in a dark matter distribution which is more extended than would be the case in the absence of galaxies, and a galaxy density profile which is more centrally concentrated than that of the halo. A simple timescale argument based on the Chandrasekhar dynamical friction formula (cf.Binney & Tremaine 1987) suggests that, on the periphery of clusters or in the largest clusters, dynamical friction should be unimportant. However, in cluster cores and larger parts of poor clusters, this timescale can be comparable to or less than a dynamical time.

The effect of such friction on the structure of the dark matter is small. If galaxies and dark matter both have the same initial specific energy, and if each galaxy loses a fraction k of its initial specific energy through dynamical friction, the specific energy of the dark matter is boosted by a factor $(1 + kM_{gal}/M_{DM})$. In rich clusters, galaxies typically account for perhaps 6% of the total mass. If baryons make up 30% of clusters — more than suggested by analyses of their mean properties (Evrard 1997) — then $M_{gal}/M_{DM} \simeq 0.085$. In this extreme case, even if galaxies lose as much as 25% of their specific energy through dynamical friction, the effect on the dark matter is only 2%. Integrating over the fits to the two–fluid and ejection ensembles' mean dark matter density profiles confirms that the total and specific energy differences between the two are less than a couple of percent. Such an energy gain by the dark matter is insignificant, and at any rate may be swamped by energy lost heating the ICM through the varying gravitational potential during collapse and relaxation. However, while the effect upon the dark matter should be weak even if the galaxies lose a large fraction of their kinetic energy, the actual magnitude of effect upon the galaxies is unclear.

A possible signal of dynamical friction is the presence of velocity bias in the cluster, $b_v < 1$, where $b_v = \sigma_{gal}/\sigma_{DM}$ is the ratio of galaxy to dark matter velocity dispersions. We examine the evolution of b_v for our simulated clusters, constructing velocity dispersions by averaging over all the galaxies or dark matter within r_{170} , in three dimensions. For individual clusters, the instantaneous value of b_v undergoes strong fluctuations depending upon the dynamical state of the cluster at that time. Even so, the value of the bias parameter is only slightly above unity (up to 1.05) for brief periods, and for only a few runs. We attempt to average out the noise associated with individual clusters by showing in Figure 6 the evolution of b_v averaged in each time bin over the entire ensemble of ejection runs, over the six most massive runs, and the eight least massive runs. In all cases, velocity bias is clearly present. The ensemble–averaged bias parameter, time–averaged over the period from z = 0.1 to the present, is 0.84. This value agrees well with an independent determination of b_v made by Frenk $et\ al.\ (1996)$ using a self–consistent treatment for galaxy

formation within the cluster.

The curves imply a mass-dependence to the degree of velocity bias, in the sense that more massive clusters are less strongly affected. This is consistent with dynamical friction arguments, where the braking effect of the dark matter background is more efficient in low velocity dispersion environments. There is no evidence for a continued decay in the velocity bias parameter, as would result from dynamical friction. However, close examination of the b_v evolution curves for individual clusters shows that they can often be described by a moderate decay, followed by a jump in velocity dispersion. The jumps occur when additional galaxies fall into the virialized volume, boosting the velocity dispersion with their infall velocities. With such complicated evolution, it is unclear whether dynamical friction is actually taking place.

The observational status of velocity bias in clusters is unclear, primarily because σ_{DM} is, of course, not directly measurable. If we define β_{DM} as the ratio of specific energies of the dark matter and gas,

$$\beta_{DM} = \frac{\sigma_{DM}^2}{\left(\frac{kT}{\mu m_p}\right)},\tag{9}$$

and if the velocity dispersion for cluster galaxies determined from observations does not suffer from anisotropies and projection effects (and these simulations suggest that it would), then β_{spec} , the spectroscopic value determined from cluster galaxies, should be related to β_{DM} through the velocity bias parameter,

$$\beta_{spec} = \frac{\sigma_{GAL}^2}{\left(\frac{kT}{\mu m_p}\right)} = b_v^2 \beta_{DM}. \tag{10}$$

If the specific kinetic energy in dark matter and thermal energy in cluster gas are both faithful representations of the cluster potential well depth, then β_{DM} should equal unity. In this case, the determination of β_{spec} for a cluster would allow determination of its velocity bias parameter. This approach was taken by Lubin & Bahcall (1993), who examined an ensemble of clusters and calculated the average value of β_{spec} for the ensemble, with the intent of eliminating dependence on dynamical state through the average. They found $\langle \beta_{spec} \rangle = 0.97 \pm 0.04$, which suggests that little or no velocity bias is present. However, this result is subject to the validity of the assumptions noted above. Their sample of clusters demonstrated a correlation between velocity dispersion and temperature, $\sigma_{GAL} \propto T^{0.6\pm0.1}$. This result was confirmed by Bird, Mushotzky & Metzler (1995), who found $\sigma_{GAL} \propto T^{0.61\pm0.13}$ for a sample of clusters explicitly corrected for the effects of substructure. Girardi et al. (1996) also obtained a similar result, using an independent analysis designed to minimize the effects of velocity anisotropies. While consistent with $\sigma_{GAL} \propto T^{0.5}$, the power law more strongly suggested by the data implies that β_{spec} is

temperature dependent. This means that any average value of β_{spec} taken from a sample of clusters will depend on the temperature distribution of the sample, making its interpretation unclear. Furthermore, when following the evolution of an individual cluster, excursions in both β_{DM} and β_{spec} can occur as a result of mergers. Finally, the assumption that $\beta_{DM}=1$ implicitly assumes that upon infall, cluster gas thermalizes very efficiently, and retains little or no energy in macroscopic motions. Perfect thermalization is not seen in simulations; a small fraction of residual kinetic energy in the gas is routinely found. A comparison of 11 gas dynamic codes applied to a single cluster realization yields a mean and standard error $\beta_{DM}=1.16\pm0.03$ (Frenk et al. 1997). Heating of cluster gas through energy input from galaxies drives β_{DM} to lower values, but with several effects pushing values larger, a modest velocity bias could still be present. It should also be noted that the mass–dependence of velocity bias noted above pushes in the direction of a relation steeper than the virial prediction $\sigma_{GAL} \propto T^{0.5}$. In this sense, observational data on the σ -T relation are consistent with the presence of velocity bias.

4. The Intracluster Medium

4.1. Hydrostatic Equilibrium

The sound crossing time in cluster gas defines a timescale for the gas to respond to acoustic disturbances. For an isothermal, $\gamma = 5/3$ gas, and with parameters on the low end of rich clusters, this timecale is

$$t_{cross} = \frac{r_{170}}{c_s} = 2.0 \left(\frac{r_{170}}{1 \text{ Mpc}}\right) \left(\frac{T}{10^7 K}\right)^{-0.5} \text{Gyr}$$
 (11)

For an $\Omega=1$, h=0.5 cosmogony, a lookback time of 2.0 Gyr corresponds to a redshift of 0.12. Since X-ray clusters have been seen to much higher redshift (*cf.* Bower *et al.* 1994; Castander *et al.* 1994), it seems reasonable to expect that much of the gas in clusters should be in hydrostatic equilibrium. Because the temperature scales with radius as $T \propto r_{170}^2$ (EMN), the above timescale is independent of cluster size.

Figure 7 shows a profile of the gas radial Mach number for two-fluid runs. The ejection runs are very similar — the main difference being a modest reduction in infall velocities — so we do not show them here. The velocities are measured with respect to the velocity of the center-of-mass of the dark matter distribution, as in Figure 1. Again, as in that figure, the multiple-cluster run (20e) displays a weak infall region. The rest of the curves show infall Mach numbers, averaged over radial shells, that reach a maximum magnitude of at most 1.2. Internal to r_{170} , radial motions of the gas are quite weak. There is, however,

some modest infall of the gas occurring at r_{170} , where $\langle v_r/c_s \rangle \simeq 0.2$. This feature is what prompted EMN to suggest r_{500} as a conservative estimate of the hydrostatic boundary of clusters. Within r_{500} there are no significant radial motions of gas in either ensemble. Mass weighted mean values of the radial Mach number within r_{500} quoted by EMN are -0.022 ± 0.022 and 0.001 ± 0.016 for the 2F and EJ ensembles, respectively. The gas is in hydrostatic balance within r_{500} , and very near to it within r_{170} .

4.2. ICM Density Profiles

The gas density profiles for the individual members of both ensembles are shown in scaled fashion in Figure 8. Like the dark matter, the density profiles of the 2F runs display remarkable similarity outside $0.2r_{170}$. Although the mean profile (bold line in the figure) drops two orders of magnitude in this regime, variation about the mean is limited to $\lesssim 20\%$. Dispersion in the central gas densities is much higher, and larger by about a factor of 3 than the central variation in the dark matter in Figure 3. This difference may be physical, originating from shocks and sonic disturbances in the gas which are absent in the dark matter. Care must be taken, however, since the spatial scales involved are quite close to the minimum hydrodynamic smoothing in the experiments. Higher resolution models will be able to address this issue. For now, we note that the cluster with the most diffuse central gas (60c) has a rather violent formation history, involving strong merger activity at low redshift.

The impact of ejection on the gas density structure is dramatic. The gas in the EJ runs is much less centrally concentrated than that of the 2F ensemble. At $0.1r_{170}$, the average density is depressed by over a factor of 3. Power law fits to the mean gas density profiles in the overdensity range $100 \le \rho_{gas}/(\Omega_b \rho_c) \le 3000$ (the overdensity range fitted for the dark matter) produce logarithmic slopes of -1.75 (EJ) and -2.34 (2F).

The difference in the mean profile values is driven primarily by low temperature clusters with ejection. Self-similarity across the mass spectrum probed by the experiments is strongly broken in the EJ ensemble; there is a systematic change in ICM structure between low and high mass clusters. Direct evidence for this is shown in Figure 9, where we plot values of α_{GAS} from fits to the standard profile, Equation 1, against the mean, mass weighted cluster temperature T within r_{170} for both ensembles. Mean values of α_{GAS} for the two ensembles are listed in Table 5, along with means for clusters hotter and cooler than 4 keV. The 2F models show no apparent trend with temperature, whereas the EJ clusters tend to smaller values of α_{GAS} , meaning more extended gas distributions, at lower T. The trend in α_{GAS} with T exhibited by the models with galactic winds agrees well with

the observed behavior of β_{fit} with T (Mohr & Evrard 1997) and appears consistent with semi–analytic treatments of galactic wind input (Cavaliere, Menci & Tozzi 1997).

The larger extent of the gas in the EJ clusters results from the work done by the wind energy dumped into these systems. The trend with temperature results from the fact that the work done in small clusters represents a larger fraction of their overall energy budget. We next consider the energetics of the ICM.

4.3. Energetics and Temperature Profiles

Figure 10 shows the mass weighted temperature within r_{170} against mass M_{170} within that radius for the two ensembles. In contrast to the density structure, the striking aspect of the T-M relation is its relative lack of sensitivity to galactic feedback. The 2F ensemble is well fit by the solid line $T_{2f}(M) = 4.0(M/10^{15} \mathrm{M}_{\odot})^{2/3}$ keV, while the EJ ensemble has a slightly shallower slope (0.62) and modest ($\lesssim 20\%$) upward displacement within the range of total masses explored. The dotted line in Figure 10 shows the expectation for the ejection run temperature T_{ej} based on assuming the wind energy is thermalized and retained within r_{170} . In this case, energy accounting yields (White 1991)

$$T_{ej}(M) = T_{2f}(M) + f_{wind} T_{wind}$$
(12)

where $T_{2f}(M)$ is the relation from pure infall, f_{wind} is the ICM gas fraction injected by winds and T_{wind} is the effective wind temperature defined in §2. The models display no systematic trend of f_{wind} with temperature, so for the purpose of illustration we use a constant value $f_{wind} = 0.22$. The expected temperatures exceed the measured values over all masses, considerably so at the low mass end.

The wind energy is not retained as heat in the ICM. Rather, it is used to do work in effectively lifting the gas within the dark matter dominated potential. To substantiate this statement, we calculate an estimate of the work done on the gas in each run by comparing the final states of gas in each 2F/EJ realization pair. Since the dark matter which dominates the mass distribution is nearly identical in the two runs, we can make an "instantaneous" approximation of the work done by integrating the change in gravitational potential energy associated with lifting a gas element from its final radius in the 2F realization to its final radius in the EJ realization. Summing, in a Lagrangian fashion, over radially ordered gas mass shells (taking into account the small reduction in gas mass due to galaxies) produces an estimate of the total work required to perturb the 2F gas distribution into the EJ configuration for each cluster. This estimate of the work required can be compared against a similarly approximate, "instantaneous" estimate of the wind energy input input

by galaxies within r_{170} , $E_{inp} = 3/2M_{gal}kT_{wind}$, where M_{gal} is the galaxy mass within r_{170} .

Figure 11a shows the result of this exercise. The agreement between these two "instantaneous" measures is quite good for most of the clusters. There is a systematic trend apparent; the slope of the points is evidently steeper than unity. We do not fully understand the cause of this steepening, but speculate that it may be connected to the difference in formation histories discussed in §3. Given the approximate nature of this calculation — assuming a static potential well when, in reality, heating of the gas occurred within the evolving potential over nearly a Hubble time — it is perhaps surprising that the agreement for most clusters is as good as it is. In poor clusters, the estimated work done exceeds the total thermal energy of the cluster gas affected, as shown in Figure 11b. For systems with total mass $M_{170} \lesssim 3 \times 10^{14} {\rm M}_{\odot}$ ($T \lesssim 4~{\rm keV}$), the work estimate is comparable to, and in a few cases exceeds, the thermal energy of the gas. Given the magnitude of the input energy, it is remarkable how little net thermal heating occurs, as displayed in Figure 10.

How much is the internal temperature structure affected by winds? Figure 12 shows the temperature profiles for the members of both ensembles at z=0.02, scaled by a fiducial virial temperature,

$$T_{170} = \frac{GM_{170}}{2r_{170}} = 7.57 \times 10^6 \left(\frac{r_{170}}{1 \text{ Mpc}}\right)^2 (1+z)^3 K$$
 (13)

There are clear structural similarities in the temperature profiles of the two samples; both display approximately isothermal behavior within half the virial radius followed by a drop to about half the central value at r_{170} . There is a fair amount of dispersion at small radii and evidence for a modest central temperature inversion in some of the 2F systems. Such a temperature inversion may be expected from the shape of the dark matter velocity dispersion profiles; the density profile is shallower than r^{-2} at small radii.

There are some structural differences as well. The EJ profiles are slightly ($\sim 25\%$) hotter in the central regions than the 2F models. This offsets the lowered density in these models and maintains hydrostatic balance. The central pressures in the EJ runs are smaller by factors of 2-3 than their 2F counterparts, but the thermal pressure gradient supporting the gas $(-\nabla P/\rho)$ is similar in the models. One observable consequence of ejection is a slightly steeper temperature profile, a feature for which there appears to be some empirical support from ASCA observations of clusters (Markevitch 1997).

Note that constructing temperature profiles by averaging over spherical shells can mask significant structure in the temperature distribution. For example, EMN present in their Figure 1 a highly irregular projected temperature map for a simulated cluster which, when averaged over three–dimensional shells or two–dimensional annuli, appears to have an

isothermal temperature profile.

Finally, we turn to the energetics of the ICM with respect to the dark matter. Figure 13 shows the distribution of values of β_{DM} , defined by Equation (9), measured within r_{170} for the two ensembles. We also construct a second set of values for β_{DM} for each ensemble, where the temperature is replaced by a total specific energy,

$$T \to T + \frac{\mu m_p \sigma_{gas}^2}{k},\tag{14}$$

to take into account the bulk motions (including rotation) and residual velocity dispersion of the gas caused by mergers and infall. The figure shows average values for β_{DM} for each data set. Because most of the wind energy goes into redistributing the gas, the shift in the mean β values between the EJ and 2F models is only 10%, comparable to the effect of including gas kinetic energy. Note also that if β_{DM} correlates with cluster temperature, as may be true for the observed β_{spec} , then our average values of β_{DM} depend on the cluster sample used. The important point here is not the exact values of these averages, but the relationships between them.

4.4. Iron Abundances and Abundance Gradients

The gas ejected by our "galaxies" is metal enriched. The distribution of metals in the ICM of our simulated clusters can thus be examined and compared with observations. Although predictions for the metal distribution are a feature unique to the ejection models, the predictions themselves are not unique, but depend on the choice of ejection history, as shown in Paper I.

We noted above that the gas distribution is more extended than the dark matter distribution in the ejection runs, with -1.75 as the best-fit power law slope at overdensities $100 \le \rho_{gas}/(\Omega_b \rho_c) \le 3000$. Meanwhile, in Figure 5, we saw that the values of α_{GAL} from fits to the galaxy number density profiles for individual runs were typically significantly higher, with only a small overlap in range of values. The gas is thus considerably more extended than the galaxy distribution. In Paper I, we showed how this can lead to an abundance gradient; the ejected, enriched gas traces the galaxies, and thus has a gradient with respect to primordial gas. Figure 14 shows that such a gradient is generally seen in the runs from about x = 0.15 out to the virial radius.

The flat metallicity profiles at smaller radii are not induced by any gravitational or hydrodynamic force resolution effects. Since resolution limits flatten the gas density profile at a larger radius than the galaxies, we would expect this to actually steepen the gradients near the center. Instead, the flattening is due to the mixing of metals at the time of gas particle ejection, which effectively acts as a diffusive term. Many gas particle ejections take place at radii below $0.1\ r_{170}$, and the core gas consequently undergoes many such mixing events. This was noted in Paper I (Figure 5b), where we showed that a model with no mixing evidenced a steeper abundance profile at small radius. An ejection model different from the one used here, in which the metal enrichment took place at earlier times, was also shown in Paper I to exhibit a flatter central abundance profile; this occurs because the difference in profiles between galaxies and gas was not yet large when the enrichment took place.

Data on abundance gradients from real clusters are only now becoming available through observations with the ASCA satellite. These data suggest that clusters sometimes have gradients and sometimes do not and that poorer systems are more likely to show evidence for an abundance gradient (Mushotzky 1994; Xu et al. 1997). Splitting our sample into high—mass and a low—mass subsets reveals no substantial difference in their gradients, as shown by the dotted and dashed lines in Figure 14.

Recall that the abundances in Figure 14 are scaled by the wind abundance. If the wind abundance is constant in time, its absolute value will not affect the shape of the abundance gradient. Similarly, a change in the total quantity of mass blown out of galaxies will not change the shape of the gradients, as long as the ejection rate remains flat. What will affect the gradient shape is if the metallicity of the wind or the ejection rate from galaxies vary with time. If the observations continue to support weak abundance gradients in rich clusters, then the discrepancy between these simulations and the observations implies that an ejection model in which the enrichment and heating took place predominantly at early times would be more appropriate.

By late times, the gradient between galaxies and gas that we see in our simulations should be present in both low–mass and high–mass clusters. Late–time enrichment should thus result in abundance gradients for both mass ranges. However, since low–mass systems form earlier in hierarchical structure models, early–ejection models would enrich the ICM when a galaxy/gas gradient is in place for low–mass clusters, but not for the high–mass clusters we see at low redshift. This would explain such an observational distinction. There is some evidence from observations of Abell 370 (z=0.37) that enrichment takes place primarily at early times (Bautz et al. 1994); the case for this is strengthened by the ASCA detection of significant quantities of neon, silicon, and other heavy elements in the ICM (Mushotzky et al. 1996) in quantities which imply injection of Type II supernova enriched gas rather than Type I. This, in turn, implies that the feedback took place early in the lifetime of cluster galaxies. We await additional ASCA and upcoming AXAF data, as well

as simulations with ejection based on well motivated star formation histories, to clarify this issue.

5. A Model for ICM Structure and the Core Radius Question

The traditional formalism used in describing the cluster gas distribution is the hydrostatic isothermal β -model, reviewed in the Appendix. However, it is somewhat disconcerting that the fundamental assumptions upon which the β -model is based are probably wrong. In particular, despite the presence of cores in X-ray images, there is no evidence for the presence of a core in cluster potentials examined through gravitational lensing observations, and simulations of clusters in both CDM and scale-free cosmologies show no core in the underlying dark matter distribution. The success of the model in fitting X-ray surface brightness profiles may be due to having three free parameters in the fitting function, when there are three basic features to fit in the data — an amplitude, a scale length to define curvature, and a large radius slope. In addition, the choice of cluster center is often adjusted to provide the best fit, introducing additional degrees of freedom. The success of the β -model profile function in modelling the gas distribution need not require that its underlying assumptions about the form of the potential be valid.

A second model can be constructed from what we learned in the previous section on the dark matter density. The one-parameter form introduced by NFW provides a good fit to the dark matter mean density profile over all resolved radii; integrating to find the dark mass within a given radius, we have

$$M_{DM}(\langle x \rangle) = 4\pi \rho_c r_{170}^3 \Delta \lambda^3 \left[\ln \left(1 + \frac{x}{\lambda} \right) - \left(\frac{x}{\lambda} \right) \left(1 + \frac{x}{\lambda} \right)^{-1} \right]$$
 (15)

where recall that $x = r/r_{170}$, the radius of interest as a fraction of our fiducial virial radius. This gives the mass within a scaled radius x, and thus within a physical radius $r = xr_{170}$. If we make the assumption that the dark mass essentially determines the cluster potential (approximately true in our simulations where the baryon fraction of the simulation volume is 10%), we can rewrite this expression as

$$M(\langle x) = M_{170} \frac{\left[\ln\left(1 + \frac{x}{\lambda}\right) - \left(\frac{x}{\lambda}\right)\left(1 + \frac{x}{\lambda}\right)^{-1}\right]}{\left[\ln\left(1 + \frac{1}{\lambda}\right) - \left(1 + \lambda\right)^{-1}\right]},\tag{16}$$

Here $M_{170} = \frac{4\pi}{3} r_{170}^3 \times 170 \rho_c$ is the mass within r_{170} . For an isothermal gas in hydrostatic

equilibrium in the potential defined by this mass profile, we then have

$$\frac{1}{\rho_g} \frac{d\rho_g}{d\left(\frac{x}{\lambda}\right)} = -K\left(\frac{x}{\lambda}\right)^{-2} \left[\ln\left(1 + \frac{x}{\lambda}\right) - \left(\frac{x}{\lambda}\right) \left(1 + \frac{x}{\lambda}\right)^{-1} \right] \tag{17}$$

where ρ_g is the local gas density, and the constant K is

$$K = 4\pi G \rho_c r_{170}^2 \left(\frac{kT}{\mu m_p}\right)^{-1} \Delta \lambda^2 \tag{18}$$

$$= \frac{G}{\lambda r_{170}} \left(\frac{kT}{\mu m_p}\right)^{-1} \frac{M_{170}}{\left[\ln\left(1 + \frac{1}{\lambda}\right) - (1 + \lambda)^{-1}\right]}$$
(19)

$$\simeq \frac{2\beta_{DM}}{\lambda \left[\ln\left(1+\frac{1}{\lambda}\right)-\left(1+\lambda\right)^{-1}\right]},\tag{20}$$

where here we have written $\sigma_{DM}^2 \simeq GM_{170}/2r_{170}$. In the absence of any significant post–infall heating or cooling of the intracluster gas, we expect the gas temperature to reflect the potential well depth, and thus $\beta_{DM} = 1$. Note that even without such additional physics, we do not expect β to equal unity locally, because we have assumed the gas to be isothermal, while we have shown earlier that this potential generates velocity dispersion profiles which are not strictly isothermal. However, K depends only on the global value; we consider the impact of such local deviations upon the global value to be small, and make this assumption in the interests of simplicity.

Integrating over a range in radii from x_1 to x gives

$$\ln\left(\frac{\rho_g\left(x\right)}{\rho_g\left(x_1\right)}\right) = K\left(\frac{x}{\lambda}\right)^{-1} \left[\ln\left(1 + \frac{x}{\lambda}\right) - \left(\frac{x}{x_1}\right)\ln\left(1 + \frac{x_1}{\lambda}\right)\right]. \tag{21}$$

This can be rearranged to give

$$\rho_g(x) = \rho_g(0) \exp\left\{K\left[\left(\frac{x}{\lambda}\right)^{-1}\ln\left(1 + \frac{x}{\lambda}\right) - 1\right]\right\}$$
(22)

Clusters in this two-component model are essentially a two-parameter family, determined by λ and T. The latter sets K through Equation (20). Given K, the normalization ρ_g (0) is determined by the total gas content of the cluster.

In a cosmological setting, the shape parameters λ and T are not formally independent, as they are both related to the cluster mass. This implies that clusters are essentially a one–parameter family, with internal structure determined by their mass. However, one must be cautious not to oversimply the picture. First, as noted before, there is considerable

scatter in values of λ at fixed mass — Tormen, Bouchet & White (1997) quote a factor of 2 at the 2σ level — which presumably arises from particular differences in clusters' dynamical histories. Also, scatter in the relation between temperature and mass of 10-20% arise from mergers (EMN), and other heating and cooling mechanisms may increase this scatter. Finally, the gas is not exactly isothermal, as assumed in the model. Nevertheless, we present this model, if only as an alternative to the standard β -model. A clear advantage over the latter is that the potential assumed in deriving Equation 22 is motivated by direct simulation of hierarchical clustering.

Like the β -model profile, Equation 22 has zero logarithmic derivative at the origin. At the β -model profile's core radius, the density has dropped to $\rho_{GAS}(0)/(2^{3\alpha_{GAS}/2})$, or slightly less than half its central value for observed values of β . If we define a core radius $x_{1/2}$ for our density profile as the radius at which the gas density drops to half its central value, we have

$$\left(\frac{x_{1/2}}{\lambda}\right)^{-1} \ln\left(1 + \frac{x_{1/2}}{\lambda}\right) = 1 - \frac{\ln 2}{K}.$$
 (23)

This is a transcendental equation for $x_{1/2}$ as a function of λ . For the value of $\lambda=0.154$ from the fit to the mean dark matter profile, and for the an approximate $\beta_{DM}=1.17$ for the two-fluid ensemble, we have K=13.2, which in turn implies $x_{1/2}=0.11\lambda=0.017$. For a cluster with a 3 Mpc virial radius, this corresponds to a core radius for the gas of 51 kpc, too low to compare favorably with observations. Alternately, using the definition of K earlier, a core radius $x_{1/2}\simeq 0.1$ (corresponding to gas core radii 100–400 kpc) implies $\lambda\simeq 0.6$, much larger than is seen in the simulations.

Figure 15 shows the ICM mean density profile for the ensemble. The large dispersion in central values is reflected in the large error bars for the central points. The vertical lines denote the values of the central SPH smoothing length for the members of the ensemble. Also shown is a fit to Equation 22. The success of the fitting function is quite striking, but the best–fit $\lambda = 0.26$ is inconsistent with the best–fit $\lambda = 0.154$ extracted from the mean dark matter profile. For contrast, the profile for $\lambda = 0.154$ is shown as a dashed line; the normalization for this curve is set by the average baryon fraction within x=1 for the ensemble. The core radius $x_{1/2}$ produced by the best–fit profile with $\lambda = 0.26$ is 0.034, still too small compared to observations, although better than the curve inferred from the dark matter distribution.

In Section III, we established that the NFW functional form provided a good description of the dark matter profile. Earlier in this section, we showed that the gas in the simulations can be thought of as isothermal and in hydrostatic equilibrium. And yet here, the gas density profile that theoretically should be a simple consequence of these facts is found to conflict with the gas density profile in the simulations. Why does the model fall

short with the gas, when it succeeds with the dark matter and when the assumptions about the gas upon which it is based seem valid? To answer this, we first note that the shape of Equation (22) depends both on λ and K, which is determined by the temperature T through the hydrostatic equation. Figure 13 indicates that post-infall thermalization of cluster gas is incomplete and that modest residual bulk motions exist in the gas. In this case, the gas temperature alone slightly underestimates the degree of pressure support. Incorporating these motions into an effective temperature, Equation (14), leads to a decrease in K and a gas distribution which is more extended than that derived from the thermal temperature alone. From Figure 13, using $\beta_{DM} = 1.03$ instead of $\beta_{DM} = 1.17$ results in the dash-dotted curve shown in Figure 15. (Again, the normalization comes from forcing the baryon fraction to the average value for the ensemble). At large radius, the agreement with data from the simulations is quite good. Since bulk motions should be included as a source of support, this curve is the one of interest. Our question has therefore changed: why does the theoretical prediction based on the potential and the complete energy budget of the ICM overestimate the central gas density when constrained to accurately describe the gas density at large radius? Why is the gas more extended in the simulations than is predicted?

To address this, we fit the gas density profiles of individual two-fluid runs to the β -profile and extracted core radii. The top row of Figure 16 shows the distribution of core radii obtained, the relation between the resulting values of r_c and the corresponding clusters' virial radii, and between r_c and the numerical parameters ϵ (the gravitational softening) and h_{cen} , the SPH smoothing length at the cluster center. Of principal importance is the latter. The cluster core radius resulting from a fit to the gas density is typically three times the central value of the SPH smoothing length. This is the approximate effective width of the smoothing kernel used in the simulations; when volume-weighted, the kernel drops to 10% of its maximum value at 2.2h; it drops to 1% at 2.8h and 0.1\% at 3.2h. We argue therefore that the theoretical model, when the entire ICM energy budget is considered, provides a good description of the large-radius behavior of the gas density in the simulations. Its failure to compare well to the simulations at smaller radii largely reflects the fact that the gas density cores seen in the simulations are principally numerical in origin. Since the hydrodynamical resolution in these simulations is comparable to most other studies, and since no physics beyond shock heating exists in such simulations to raise the adiabat of cluster core gas, we suggest that gas cores seen in these other studies are also numerical in origin. Support for this position is found in recent numerical studies by Anninos & Norman (1996), which were not able to converge to a well-defined gas density core as resolution improved. It remains possible that physical effects contribute to the difference between the model and simulated core profiles. In particular, deviations from isothermality and small amounts of core rotational support are present in the simulated clusters but not in the

analytic model.

In the right-hand-side of Figure 15, we compare the NFW gas density profile to the mean profile for the ejection ensemble. Once again, the best-fit does an excellent job of reproducing the mean profile, but with a scale length of $\lambda = 0.329$, much larger than the scale in the potential. The dashed and dash-dotted lines are as before; thus, the dash-dotted line contains the bulk motions of the gas indicated in Figure 13, and is the true prediction of the theoretical model. Once again, the core in the real density profile is more pronounced than that of the model, although not as severely as for the two-fluid runs. The ICM in the ejection runs has experienced post-infall heating, slightly raising ICM gas temperatures over pure infall runs, and resulting in β_{DM} decreased typically by 8%. This translates into a more extended gas distribution. However, as is seen in the figure, the heating provided by our ejection model is not sufficient alone to account for the ICM cores we see in the simulation runs; numerical effects must still be important. This is illustrated by the vertical lines on the figure which mark the value of h_{cen} for the various members of the ensemble; again, $3h_{cen}$ approximately marks the range of interest, where deviation from the theoretical prediction begins to be important. The bottom row of Figure 16 shows that the cores still have a lower limit of $3h_{cen}$, but now extend to larger radii as well. Numerics still dominate the core radii in the ejection ensemble, but the entropy introduced by winds is beginning to play a role. We conclude that the model employed here is not sufficient to generate the depressed central densities and cluster core radii necessary to compare to real systems.

We could have predicted this result. Equation 23 gives the dependence of the core radius in this model on the parameter K. For $\lambda=0.154$, correcting K by a factor of 1.03/1.17=0.88 (the ratio of values of β , or of temperatures) merely raises the size of the core radius by 10%. While additional sources of heating raise the temperature, thus lowering K and thus increasing $x_{1/2}$, the increase we need is extremely large. To raise $x_{1/2}$ to values comparable to real clusters (i.e. $x_{1/2}=0.1$), the temperature must be boosted by a factor of three or four; such a model is physically implausible and observationally unjustified.

We remain without an explanation of the gas cores of real clusters. The cores predicted by the analytic model, based upon the application of the NFW profile to our simulated mass distributions, appear too small to explain those observed in real clusters. One possibility is that the mass density profile for real clusters is typically shallower than indicated by the NFW profile here, in the sense that it approaches r^{-2} at a larger radius than occurs in these simulations. This would be the case if the parameter λ , the scale radius of the NFW model in units of r_{170} , were significantly larger than is seen here, as may be the case for CDM models with lower values of Ω_o (Navarro, Frenk & White 1997). Another possibility, however, is that additional physics, such as magnetic fields, provide an important source of support at small radius. This view is bolstered by measurements of Faraday rotation in X–ray clusters (Taylor, Barton & Ge 1994; Ge & Owen 1994) and comparisons of X–ray and lensing mass measurements for cluster core regions (Loeb & Mao 1994; Miralda-Escude & Babul 1995). Finally, winds with energy output concentrated at early times may raise the central entropy to a higher level than that seen in the models used here, and this may be sufficient to generate core radii of the requisite scale. Accurate modelling of these effects awaits future simulations.

6. Relative Structure and the Baryon Fraction

We summarize in Table 6 what we have learned about the relative extents of gas and dark matter by showing the results of power law fits to the outer slope of the mean ensemble density profile for each fluid in the two ensembles.

For the dark matter, we do not quote separate values for the two ensembles as their outer slopes are not significantly different. Small number statistics do not allow a comparable fit for the galaxies; the range of values quoted in Table 6 come from Figure 5. We can show their relative extent more clearly by displaying in Figure 17 the *cumulative* density measure — that is, the fraction of the virial mass in each component found within a given radius. This figure illustrates that the gas with or without feedback is more extended than the dark matter, and that the difference is significantly enhanced by the energy input from galactic winds. At small radii, the dark matter in the ejection ensemble is typically slightly more extended than the corresponding dark matter in the two–fluid runs; however, the difference is quite small. Finally, the galaxy profile is more centrally concentrated than any of the other components. The half–mass radii for each of the fluids displays this hierarchy.

As a consequence of the extended nature of the gas distribution, the mean, enclosed baryon fraction is reduced relative to the global value Ω_b/Ω_0 at radii interior to the virial radius. In the EJ ensemble, the ICM mass fraction is further reduced by the baryons incorporated into galaxies. The amplitude of this reduction within radii encompassing density contrasts $\delta_c = 170$ and 500 is shown in Figure 18, where we plot the normalized, local baryon fraction of each component, defined by $\Upsilon_X = f_X(\Omega_b/\Omega_0)^{-1}$ with $f_X = M_X(\delta_c)/M_{tot}(\delta_c)$ the mass fraction of component X (gas, galaxies, total baryons) within the radius encompassing density contrast δ_c .

The ensemble without ejection displays modest diminutions, $\langle \Upsilon \rangle = 0.94$ within r_{170} and 0.91 within r_{500} , with no apparent trend with cluster size. The slight differences in formation history between low and high mass systems, which produces the modest structural differences discussed in §III, is not apparent in the behavior of gas mass fraction with temperature. The ensemble with ejection exhibits markedly different behavior. Although the galaxy mass fraction is insensitive to cluster size, the ICM mass fraction is noticeably reduced in lower temperature systems, particularly those with $T \lesssim 4$ keV. The magnitude of the effect depends on the region under consideration. At $\delta_c = 170$, there is a 30% fractional drop (from $\Upsilon_{gas} = 0.75$ to 0.55) between 10 and 1 keV, whereas the effect is nearly a factor two drop at $\delta_c = 500$. The larger effect at higher densities or smaller radii reflects the difference in ICM structure between low and high T objects displayed in Figure 9; lower temperature clusters in the ensemble have less centrally concentrated gas distributions. At smaller radii or higher density contrasts, the disparity in gas fractions between low and high T clusters increases.

For high temperature clusters ($T \gtrsim 4 \text{ keV}$), the total baryon fraction within r_{170} is nearly unaffected by galactic winds. There are, however, modest structural differences in the gas distribution within this radius, as indicated from the reduction in α_{gas} from values ~ 0.89 to ~ 0.79 (Table 5). The work associated with the wind energy injected into rich clusters is thus used to redistribute gas within r_{170} , but causes little or no "spillover" at this radius. This is not the case for the low temperature clusters, where the considerable wind energy results in a more dramatic redistribution of the gas extending beyond r_{170} . Still, the diminution of the total baryon fraction is not catastrophic, even at low temperatures. A crude fit to the total baryon fraction $\Upsilon(T)$ with T (in keV) for the EJ ensemble yields

$$\Upsilon(T) \simeq 1 - AT^{-2/3} \tag{24}$$

where $A \simeq 0.3$ at $\delta_c = 170$ and $A \simeq 0.4$ at $\delta_c = 500$. These are shown as solid lines in Figure 18.

We stress that the exact form and magnitude of $\Upsilon(T)$ is likely to be sensitive to the specific wind model employed. One must look for empirical and/or additional theoretical support to justify a particular model. Our particular implementation is successful at reproducing the slope of the observed X-ray size-temperature relation (Mohr & Evrard 1997), and this may indicate that our particular wind implementation is well calibrated, in terms of its energetic or entropic effects. This provides some reason to be optimistic that the predicted form for $\Upsilon(T)$ in Equation 24 may apply to real clusters. Future efforts employing more realistic wind ejection histories are needed to clarify this issue.

7. Summary

We investigate the structure of clusters in a CDM universe using multi-component, numerical simulations spanning a factor of 50 in cluster mass. Dark matter, intracluster gas and galaxies are included in a set of models designed to explore the role of feedback of mass and energy into the ICM. Two principal assumptions made for the galaxy population are: (i) galaxies form at the locations of peaks in the initial density field and (ii) galaxies lose half of their initial mass via winds at a flat rate from z = 4.5 to the present.

The self–similar form for CDM cluster density profiles seen in earlier works (NFW2; Metzler 1995; Cole & Lacey 1996; Tormen, Bouchet & White 1997) provides an excellent description of the dark matter distribution in these simulated clusters. The degree of central concentration increases with decreasing cluster mass, as expected from these earlier works and from the formation history of objects in hierarchical clustering models. The characteristic scale radius for this profile appears at 0.1– $0.2~r_{170}$ in these simulations; however, Navarro, Frenk & White (1997) caution that the location of the scale radius is dependent upon the assumed value of the density parameter.

The two-fluid models, lacking winds, exhibit a self-similar gas distribution. At large radii, the gas density profile matches well the expection from hydrostatic equilibrium and the self-similar profile observed for the dark matter. The agreement at smaller radii is difficult to determine because of resolution limits. The introduction of winds raises the gas entropy above levels achieved by gravitational infall and thus produces a more extended gas distribution within the dark matter dominated potential. The effect of winds is strongest on low-mass clusters, where the energy input by winds is comparable to the total thermal energy of the gas. Thus, the self-similarity seen in the gas distribution of the two-fluid models is broken with the introduction of winds, with the gas in low temperature clusters being more strongly affected than their high temperature counterparts.

The energy input through winds is primarily spent in redistributing the gas within the potential; the effect on the gas temperatures is slight. Thus, the introduction of winds does not seem to affect the relation between ICM temperature and mass. This, in turn, supports the use of mass estimators that assume gas temperature to be simply related to potential well depth. However, the dependence of this result upon the wind model chosen remains to be determined. Detailed temperature information from X–ray satellites, combined with independent mass estimates from weak lensing analysis, can probe this relation in real clusters.

Galaxies are more centrally concentrated than the dark matter in these simulations. Part of this effect arises simply because the initial distribution of galaxies is more

concentrated than the dark matter — an artifact of considering overdense peaks as likely sites for galaxy formation. However, in addition, a persistent velocity bias between galaxies and dark matter is present in the ejection ensemble; the degree of bias correlates with cluster mass in a manner consistent with the expectations of bias induced by dynamical friction.

As the gas is more extended than the dark matter, while the galaxies are more concentrated, a gradient between galaxies and gas exists. As a result, metal abundance gradients are generic to the ejection models. However, this result is sensitive to the specific wind model used; the gradient is reduced if winds and metal enrichment occur only at high redshift. The strength of the metal abundance gradients seen in this work shows no dependence on cluster mass, which may be in contradiction with observations. The relative ordering of extents of the three fluids simulated is, however, consistent with present observations.

While energy input from feedback depresses central gas densities and causes a more extended gas distribution, the effect is not significant enough to explain observed cluster gas density cores observed in X-ray images. While cores of appropriate size are present in these simulations, they appear predominantly numerical in origin. Possible sources of X-ray cores include additional sources of support such as magnetic fields, or a change to the cluster density profile such as is expected for low- Ω cosmologies (Navarro, Frenk & White 1997). An ejection history featuring vigorous, early winds may also lead to larger cores, since the central gas entropy could be raised above that seen in the experiments presented here.

Since the low–temperature clusters simulated experience the strongest effect upon the gas density profile, estimates of the baryon fraction should be taken from high–temperature clusters whenever possible. The local baryon fraction in 10 keV clusters is approximately 90% of the global value and is insensitive to winds, while loss approaching a factor of two in gas fraction can occur in interior parts of low–temperature clusters.

This research suggests at least two directions for future numerical experiments. One is to consider the simplified evolution of gas assumed to be isentropic at some high redshift, but which is allowed to change its adiabat through shock heating and (optionally) radiative cooling at later times. Systematically varying the initial adiabat would mimic the effect of abrupt wind input of varying strength at high redshift, and would allow structural issues, such as core radii generation, to be addressed. Another approach is to increase the spatial and mass resolution in the experiments and add appropriate physics to allow galaxy formation to be modelled self-consistently within forming clusters. This is the long-term goal of such cosmological simulations, but it remains a formidable task because of the uncertainties in modeling star formation on galactic scales, the inherent complexity

of the dynamical system involved, and the large parameter space (physical and numerical) associated with the problem. There is much yet to be gained from simple models, but the problem cannot be considered "solved" until the latter approach is complete.

CAM would like to thank Tina Bird, Mary Crone, Richard Mushotzky, Julio Navarro, and Gordon Squires for useful discussions. This work was supported by the NASA Astrophysics Theory Program through grants NAGW-2367 and NAG5-2790. CAM also would like to acknowledge support from a Rackham Predoctoral Fellowship and a Sigma Xi Grant-in-Aid of Research at the University of Michigan, and the Department of Energy and NASA Grant NAG5-2788 at Fermilab. AEE acknowledges support from the CIES and CNRS during a sabbatical stay at the Institut d'Astrophysique in Paris.

A. Appendix

We provide here a brief summary of the hydrostatic, isothermal β -model (Cavaliere & Fusco-Femiano 1976, 1978; Sarazin & Bahcall, 1977). Those familiar with the model may still wish to briefly review this appendix in order to become familiar with the notation used in the paper.

The model presumes that the intracluster medium is isothermal and hydrostatic in a potential well determined by collisionless, dark matter following the density profile

$$\rho = \rho_0 \left[1 + \left(\frac{r}{r_c} \right)^2 \right]^{-3\alpha_{DM}/2}, \tag{A1}$$

where r_c is the core radius of the cluster. All the early literature on the model assumes that the collisionless matter is described by the King approximation to the isothermal sphere, meaning $\alpha_{DM} = 1$. The relevant hydrostatic equations for the gas and collisionless matter are

$$\frac{dP}{dr} = -\rho_g \frac{d\Phi}{dr},\tag{A2}$$

and

$$\frac{d\left(\rho_{DM}\sigma_r^2\right)}{dr} + \frac{2\rho_{DM}}{r} \left[\sigma_r^2 - \sigma_t^2\right] = -\rho_{DM} \frac{d\Phi}{dr},\tag{A3}$$

with P the gas thermal pressure; Φ the gravitational potential; ρ_g and ρ_{DM} the densities of gas and collisionless matter respectively; σ_r the radial velocity dispersion, and $\sigma_t = 0.5 \left(\sigma^2 - \sigma_r^2\right)^{1/2}$ the tangential velocity dispersion, of the collisionless matter. The model assumes spherical symmetry, so that $d\Phi/dr = -GM_{tot}\left(\langle r \rangle/r^2\right)$. If one then

demands isothermality (that is, that the gas temperature and collisionless matter velocity dispersion are independent of radius), one obtains

$$\frac{kT}{\mu m_p} \frac{d\rho_g}{dr} = -\rho_g \frac{GM_{tot}(\langle r)}{r^2} \tag{A4}$$

and

$$\sigma_r^2 \frac{d\rho_{DM}}{dr} + \frac{2\rho_{DM}\sigma_r^2}{r} A(r) = -\rho_{DM} \frac{GM_{tot}(\langle r)}{r^2}, \tag{A5}$$

where $A(r) = 1 - \sigma_t^2/\sigma_r^2$ is the anisotropy parameter. If we assume that the collisionless matter follows Equation A1, then the gas density has a similar functional form,

$$\rho_g(r) = \rho_{g,0} \left[1 + \left(\frac{r}{r_c} \right)^2 \right]^{-3\alpha_{GAS}/2}. \tag{A6}$$

with

$$\alpha_{GAS} = \beta_r \left(\alpha_{DM} - 2/3A(r) \right) \tag{A7}$$

and β_r is the ratio of specific energies,

$$\beta_r = \frac{\sigma_r^2}{\left(\frac{kT}{\mu m_p}\right)}.$$
(A8)

All of these parameters can depend on radius in the cluster. In the standard implementation of the β -model, one assumes $\alpha_{DM}=1$ and an isotropic velocity dispersion $\sigma_r=\sigma_t\equiv\sigma$, so A(r)=0. In this case, $\alpha_{GAS}=\beta$ of Equation 2.

The volume emissivity of thermal bremsstrahlung emission is $\epsilon_{ff} \propto \rho_g^2 T^{1/2}$; the surface brightness is then calculated from a line-of-sight integral of the square of the gas density. The functional form used by observers to fit X-ray surface brightness profiles is

$$\Sigma_x(\theta) = \Sigma_0 \left[1 + (\theta/\theta_x)^2 \right]^{-3\beta_{fit} + 1/2}, \tag{A9}$$

which is identical to the result obtained from the β -model profile if the cluster is isothermal, with $\beta_{fit} = \alpha_{GAS}$, and θ_x being the angular size of the core radius r_c at the cluster's redshift. Typically, data show $\beta_{fit} < \beta$, where the ratio of specific energies β is determined by direct spectral analysis of cluster galaxy redshifts and by X-ray spectral fitting. Various effects have been noted to explain this so-called " β -discrepancy". Since the logarithmic slope of Equation (A9) is a function of radius, $\beta_{fit} < \alpha_{GAS}$ unless the data used in the surface brightness fit extends to sufficient radius. Also, from the relation between α_{GAS} and β , α_{GAS} will be less than β if $\alpha_{DM} < 1$ or if A(r) > 0, both of which are seen in simulations (Evrard 1990a,b). Finally, if thermalization of cluster gas after infall is

incomplete, and the ICM is partially supported by residual motions, then β overestimates the ratio of specific energies, and the "effective" value of β is decreased.

The galaxies, as another collisionless fluid, should also follow this functional form, although perhaps with a different large–radius logarithmic slope to the density profile—that is, α_{qal} need not equal α_{DM} .

REFERENCES

Anninos, P., & Norman, M. L. 1996, ApJ, 459, 12.

Bardeen, J. M., Bond, J. R., Kaiser, N., & Szalay, S. 1986, ApJ, 304, 15.

Barnes, J. 1985, MNRAS, 215, 517.

Bautz, M. W., Mushotzky, R., Fabian, A. C., Yamashita, K., Gendreau, K. C., Arnaud, K. A., Crew, G. B., & Tawara, Y. 1994, PASJ, 46, L131.

Bertschinger, E. 1985, ApJS, 58, 39.

Bertschinger, E. 1987, ApJ, **323**, L103.

Biermann, P. 1978, A&A, **62**, 255.

Binney, J., & Tremaine, S. 1987, Galactic Dynamics (Princeton University Press, Princeton).

Bird, C. M., Mushotzky, R. F., & Metzler, C. A. 1995, ApJ, 453, 40.

Blumenthal, G. R., Faber, S. M., Primack, J. R., & Rees, M. J. 1984, Nature, 311, 517.

Briel, U.G, Henry, J.P. & Böhringer, H. 1992, A&A, **259**, L31.

Bower, R. G., Bohringer, H., Briel, U. G., Ellis, R. S., Castander, F. J., & Couch, W. J. 1994, MNRAS, **268**, 345.

Carlberg, R. G. 1991, ApJ, 367, 385.

Carlberg, R. G. 1994, ApJ, **433**, 468.

Carlberg, R. G., & Dubinski, J. 1991, ApJ, **369**, 13.

Carr, B. J., Bond, J. R., & Arnett, W. D. 1984, ApJ, 277, 445.

Castander, F. J., Ellis, R. S., Frenk, C. S., Dressler, A., & Gunn, J. E. 1993, ApJ, 424, 79.

Cavaliere, A., & Fusco-Femiano, R. 1976, A&A, 49, 137.

Cavaliere, A., & Fusco-Femiano, R. 1978, A&A, 70, 677.

Cavaliere, A., Menzi, N. & Tozzi, P. 1997, ApJ, 484, 21.

Cole, S., & Lacey, C. 1996, MNRAS, 281, 716.

Crone, M. M., Evrard, A. E., & Richstone, D. O. 1994, ApJ, 434, 402.

Davis, M., Efstathiou, G., Frenk, C. S., & White, S. D. M. 1985, ApJ, 292, 371.

Edge, A. C., & Stewart, G. C. 1991, MNRAS, **252**, 428.

Efstathiou, G. & Eastwood, J.W. 1981, MNRAS, 194, 503.

Efstathiou, G., Davis, M., Frenk, C. S. & White, S. D. M. 1985, ApJS, 57, 241.

Evrard, A. E. 1987, ApJ, 316, 36.

Evrard, A. E. 1988, MNRAS, 235, 911.

Evrard, A. E. 1990a, *Clusters of Galaxies*, edited by W. Oegerle, M. Fitchett, & L. Danly (Cambridge University Press, Cambridge), 287.

Evrard, A. E. 1990b, ApJ, **363**, 349.

Evrard, A. E., Silk, J., & Szalay, A. S. 1990, ApJ, **365**, 13.

Evrard, A. E., Metzler, C.A. & Navarro, J.N. 1996, ApJ, 437, 564.

Frenk, C. S., White, S. D. M., Davis, M., & Efstathiou, G. 1988, ApJ, 327, 507.

Frenk, C. S., et al. . 1997, in preparation.

Gaetz, T. J., Salpeter, E. E., & Shaviv, G. 1987, ApJ, 316, 530.

Ge, J., & Owen, F. N. 1994, A. J., 108, 1523.

Gingold, R. A., & Monaghan, J. J. 1977, MNRAS, 181, 375.

Girardi, M., Fadda, D., Giuricin, G., Mardirossian, F., Mezzetti, F., & Biviano, A. 1995, ApJ, 457, 61.

Gunn, J. E., & Gott, J. R. 1972, ApJ, 176, 1.

Ikebe, Y., Makishima, K., Ezawa, H., Fukazawa, Y., Hirayama, M., Honda, H., Ishisaki, Y., Kikuchi, K., Kubo, H., Murakami, T., Ohashi, T., Takahashi, T., & Yamashita, K. ApJ, 481, 660.

Juszkiewicz, R., Bouchet, F.R., & Colombi, S. 1993, ApJ, 412, 9.

Larson, R. B., & Dinerstein, H. L. 1975, PASP, 87, 911.

Loeb, A., & Mao, S. 1994, ApJ, 435, 109.

Lubin, L. M., & Bahcall, N. A. 1993, ApJ, 415, 17.

Metzler, C. A. 1995, Ph.D. Thesis, University of Michigan.

Metzler, C. A. 1997, in preparation.

Metzler, C. A., & Evrard, A. E. 1994, ApJ, 437, 564.

Miralda-Escudé, J., & Babul, A. 1995, ApJ, 449, 18.

Moore, B., Governato, F., Quinn, T., Stadel, J., & Lake, G. 1997, ApJ, submitted (astro-ph/9709051).

Mushotzky, R. F. 1994, *Clusters of Galaxies*, edited by J. Trân Thanh Vân, F. Durret, A. Mazure, & S. White, 167.

Mushotzky, R., Loewenstein, M., Arnaud, K., Tamura, T., Fukazawa, Y., Matsushita, K., Kikuchi, K., & Hatsukade, I. 1996, ApJ, 466, 686.

Navarro, J.N., Frenk, C.S., & White, S.D.M. 1995, MNRAS, 275, 720. (NFW1)

Navarro, J.N., Frenk, C.S., & White, S.D.M. 1996, ApJ, 462, 563. (NFW2)

Navarro, J.N., Frenk, C.S., & White, S.D.M. 1997, ApJ, in press.

Peebles, P. J. E. 1980, *The Large Scale Structure of the Universe* (Princeton University Press, Princeton).

Sarazin, C. L., & Bahcall, J. N. 1977, ApJS, 34, 451.

Takeda, H., Nulsen, P. E. J., & Fabian, A. C. 1984, MNRAS, 208, 261.

Tamura, T., Day, C. S., Fukazawa, Y., Hatsukade, I., Ikebe, Y., Makishima, K., Mushotzky, R. F., Ohashi, T., Takenaka, K., & Yamashita, K. 1996, PASJ, 48, 671.

Taylor, G. B., Barton, E. J., & Ge, J. 1994, A. J., 107, 1942.

Tormen, G., Bouchet, F.R. & White, S.D.M. 1997, MNRAS, 286, 865.

Tyson, J.A., Valdes, F. & Wenk, R.A. 1990, ApJ, **349**, 1.

West, M. J. & Richstone, D. O. 1988, ApJ, **335**, 532.

White, R. E. 1991, ApJ, **367**, 69.

White, S.D.M., Davis, M., Efstathiou, G. & Frenk, C.S. 1987, Nature, 330, 451.

Xu, H., Ezawa, H., Fukazawa, Y., Kikuchi, K., Makishima, K., Ohashi, T., & Tamura, T. 1997, PASJ, **49**, 9.

Yahil, A., & Ostriker, J. P. 1973, ApJ, 185, 787.

This preprint was prepared with the AAS IATEX macros v4.0.

- Fig. 1.— Dark matter radial velocity profiles at z=0.02 for four members of the two-fluid ensemble. Profiles are centered on the most bound dark matter particle of each cluster. Mean interior density contrast is used as the radial coordinate. The dashed lines mark the predictions of the simple spherical infall model for the virial radius and the turnaround radius.
- Fig. 2.— Dark matter density profiles for the eighteen members of the two-fluid ensemble, at z = 0.02. The vertical lines mark the value of the gravitational softening parameter ϵ for the various runs.
- Fig. 3.— (a) Rescaled dark matter density profiles for the two–fluid ensemble at z=0.02. Densities are scaled to multiples of the background (critical) density, and radii rescaled by the radius with a mean interior density contrast of 170, for each cluster. Vertical lines mark the gravitational softening for the various runs. (b) The mean dark matter profile for the two–fluid ensemble, along with three fits. The mean density profile, denoted by the points and error bars, is derived from the average value of the density contrast at that scaled radius amongst the members of the ensemble; the errorbars come from the scatter in this value amongst the ensemble. The solid line is a fit to the one–parameter density profile suggested by NFW2. The dotted line is a simple power–law fit. The dashed line is a fit to the density profile of the standard β –model form.
- Fig. 4.— Dark matter velocity dispersion and orbital anisotropy profiles for the two-fluid models at z=0.02. The top half shows dark matter velocity dispersion profiles for the eighteen two-fluid runs. The velocity dispersions have been rescaled by $\sigma_{170} \simeq GM_{170}/2r_{170}$. The bottom half shows the value of the anisotropy parameter, $A(r) = 1 \sigma_t^2/\sigma_r^2$, for the runs. The radial coordinate has been rescaled by r_{170} .
- Fig. 5.— Galaxy number density profiles for the six most massive clusters in the ejection ensemble, at z=0.02. Each radial bin holds five galaxies. The solid lines show fits to the β -model profile; the values for $3\alpha_{gal}$ shown give the large-radius logarithmic slope of the number density profile from the fits.
- Fig. 6.— Evolution of the velocity bias parameter $b_v = \sigma_{gal}/\sigma_{DM}$, averaged over the entire ejection ensemble and over high– and low–mass subsets. Time is written in terms of the endpoint of the simulations at z = 0.
- Fig. 7.— Gas radial mach number at z=0.02 for the eighteen members of the two-fluid ensemble.

- Fig. 8.— (a) Scaled two–fluid ensemble gas density profiles at z=0.02. Radii are rescaled by r_{170} and densities by the background baryon density, similar to the dark matter in Figure 3. The vertical lines here denote the values of the central SPH smoothing length for the members of the ensemble. A mean profile, defined as for the dark matter by taking an average amongst the ensemble members in Eulerian bins, is shown as a heavy solid line. (b) The equivalent profiles for the ejection ensemble. The heavy solid line again marks a mean profile for the ensemble. The heavy dashed line shows the mean profile for the two–fluid ensemble from panel(a), to facilitate comparison.
- Fig. 9.— The gas outer slope parameter α_{gas} from fits to the standard form, Equation 1, as a function of cluster temperature. Open circles are models without ejection (2F ensemble), while asterisks show models with winds (EJ ensemble). The similarity in this variable evident in the 2F ensemble is broken by the introduction of winds.
- Fig. 10.— Mass weighted cluster temperature T against mass M_{170} , both measured within the virial radius r_{170} . Symbol types are the same as in Figure 9. The solid line gives a fit to the 2F data $T_{2f}(M) = 4.0(M/10^{15} M_{\odot})^{2/3}$ keV, while the dahsed line is the mass–temperature relation expected in the ejection models if the input wind energy is retained as thermal energy (Equation 12).
- Fig. 11.— (a) Estimates of the work required to lift the gas in each cluster from its final configuration in the 2F realization to that in the EJ realization plotted against galaxy mass within the virial radius. The solid line gives the energy input by those galaxies over the course of the simulation. See text for a discussion. (b) Ratio of the work estimate to the total gas thermal energy as a function of total cluster mass. The work performed by winds is comparable to the total thermal energy in low mass, low temperature clusters.
- Fig. 12.— Scaled two-fluid ensemble temperature profiles at z = 0.02. Here temperatures are scaled by $T_{170} = (\mu m_p/k) (GM_{170}/2r_{170})$. The left-hand panel shows the results for the two-fluid ensemble, while the right-hand panel shows the results for the ejection ensemble.
- Fig. 13.— Histograms of the distribution of $\beta_{DM} = \mu m_p \sigma_{DM}^2 / kT$ for the two-fluid and ejection ensembles, both with and without correcting temperatures to account for gas specific energy in bulk motions, at z = 0.02.

Fig. 14.— Iron abundance profiles for five members of the ejection ensemble at z = 0.02. Also shown are mean profiles for the entire ensemble (heavy solid line), the high mass subset (heavy dotted line), and the low mass subset (heavy dashed line).

Fig. 15.— (a) z=0.02 mean gas density profile for the two-fluid ensemble. Error bars come from the dispersion in each Eulerian bin amongst members of the ensemble. The solid line is a fit to the form predicted by the NFW model with the assumptions of hydrostatic equilibrium and isothermality. The dashed line is the prediction of the NFW model for the scale length of the potential ($\lambda=0.154$) found through studying the mean dark matter distribution, without including gas motions in the pressure support. The dash-dotted line is the prediction of the generalized NFW model for the known form of the potential including gas motions in the pressure support term. These last two lines are normalized to produce the correct amount of gas within r_{170} . (b) The equivalent plot for the ejection ensemble. Again, the solid line is a direct fit to the mean profile; the dashed line is the prediction of the NFW model assuming the scale length found in the potential; and the dash-dotted line is the prediction of the model when including bulk motions in the temperature. Finally, the direct fit to the two-fluid model points is shown here as a dotted line, to facilitate comparison.

Fig. 16.— Histograms of gas density core radii at z = 0.02, for both ensembles. Values of the core radius r_c are taken from fits to the β -model form. Shown are absolute values of r_c , as well as values scaled in terms of r_{170} , the gravitational softening, and the SPH smoothing length at the cluster center.

Fig. 17.— Enclosed mass profiles for the various cluster components at z = 0.02. Each line corresponds to the fraction of the mass in that component at r_{170} that is enclosed within radius r. The clusters in each ensemble were renormalized to their values of r_{170} and "stacked" on top of each other to produce a characteristic curve for each component in the ensemble. Components are marked by different lines: two–fluid ensemble dark matter (solid); two–fluid ensemble gas (dotted); ejection ensemble dark matter (short–dashed); ejection ensemble galaxies (dot–dashed).

Fig. 18.— Local baryon fractions, normalized to the cosmic ratio, within two different density contrasts displayed versus mass—weighted temperature. Open circles show the 2F ensemble results, while components within the EJ ensemble are shown individually (filled triangles: gas; filled circles: galaxies) and in total (asterisks). Solid lines show fits to the EJ total, Equation 24 at each density contrast. The short—dashed line in the $\delta_c = 500$ panel shows $\delta_c = 170$ result; the baryon fraction decreases toward smaller radii or larger density contrasts. The long—dashed line at unity reflects a local baryon fraction equal to the cosmic mean value. All clusters are baryon deficient. The EJ ensemble shows a dependence of the local baryon fraction on temperature but, at high temperatures, the total baryon content is similar to that in the models without ejection.

Table 1. General Simulation Parameters

Parameter	Value
Comoving Box Length L (Mpc)	20, 25, 30, 40, 60
Total Mass in Box (M_{\odot})	$4.44 \times 10^{15} \left(\frac{L}{40 \text{ Mpc}}\right)^3$
Number of Dark Matter Particles	32768
Mass per Dark Matter Particle (M_{\odot})	$1.22 \times 10^{11} \left(\frac{L}{40 \text{ Mpc}} \right)^3$
Number of Gas Particles in Two–Fluid Runs	32768
Mass per Gas Particle (M_{\odot})	$1.35 \times 10^{10} \left(\frac{L}{40 \text{ Mpc}} \right)^3$
Initial Redshift	9
Timestep (yr)	1.29×10^{7}
Initial Temperature of Gas	$10^4 \mathrm{K}$
Specific Energy of Wind (L_{wind}/\dot{M})	$1.37 \times 10^8 \ \mathrm{K}$

Table 2. Final Characteristics of Two-Fluid Models

Run	M_{170}	$\sigma_{DM,170}$	T_{170}
	$({ m M}_{\odot})$	(km s^{-1})	(K)
b20bn	8.34×10^{13}	365	8.75×10^{6}
b20cn	1.29×10^{14}	435	1.15×10^7
b20en	8.36×10^{13}	353	7.81×10^{6}
b20fn	1.16×10^{14}	462	1.28×10^{7}
b25an	2.84×10^{14}	597	2.00×10^7
b25bn	2.79×10^{14}	564	2.08×10^{7}
b25cn	3.31×10^{14}	576	2.07×10^7
b25dn	2.60×10^{14}	564	2.05×10^7
b30an	4.59×10^{14}	665	2.84×10^{7}
b30bn	4.94×10^{14}	721	3.10×10^7
b30cn	4.66×10^{14}	667	2.69×10^7
b30dn	4.57×10^{14}	632	2.64×10^{7}
b40an	1.14×10^{15}	881	4.94×10^7
b40bn	9.20×10^{14}	818	4.48×10^{7}
b40cn	1.04×10^{15}	942	5.28×10^7
b60bn	2.61×10^{15}	1120	8.55×10^7
b60cn	3.92×10^{15}	1420	1.12×10^8
b60dn	3.59×10^{15}	1310	9.58×10^7

 ${\it Table 3.} \quad {\it Final Characteristics of Ejection Models}$

Run	f_{gas}	N_{GAL}	$N_{GAL} \left(< r_{170} \right)$	$T_{170} (K)$
b20b	0.914	24	8	1.02×10^7
b20c	0.879	35	16	1.31×10^7
b20e	0.921	26	11	9.29×10^{6}
b20f	0.913	39	15	1.34×10^7
b25a	0.912	41	31	2.22×10^7
b25b	0.887	48	31	2.24×10^7
b25c	0.881	56	36	2.49×10^7
b25d	0.895	50	24	2.17×10^7
b30a	0.879	79	46	3.04×10^{7}
b30b	0.904	64	42	3.25×10^7
b30c	0.899	78	39	3.03×10^7
b30d	0.886	79	40	2.93×10^{7}
b40a	0.875	128	60	5.47×10^7
b40b	0.878	128	55	4.74×10^7
b40c	0.894	115	53	5.43×10^7
b60b	0.842	201	72	9.21×10^7
b60c	0.849	195	103	1.19×10^{8}
b60d	0.851	189	100	1.01×10^{8}

Table 4. Dark Matter Density Profile Fits

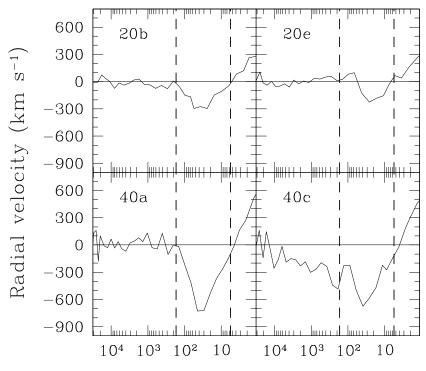
Ensemble	$_{\lambda}^{\mathrm{NFW}}$	eta –model $lpha_{DM}$	Power-Law Slope α $100 \le \rho/\rho_{back} \le 3 \times 10^3$
All Runs	0.154 ± 0.008 $\chi^2/\nu = 0.53$	0.826 ± 0.018 $\chi^2/\nu = 0.39$	$2.39 \pm 0.08 \chi^2/\nu = 0.24$
High Maga	$q = 0.99$ 0.176 ± 0.01 $\chi^2/\nu = 0.75$	$q = 0.99$ 0.816 ± 0.018 $2^{2}/v = 0.60$	$q = 1.0$ 2.35 ± 0.07 $\chi^{2}/\nu = 0.53$
High Mass Subset	q = 0.85	$\chi^2/\nu = 0.60$ $q = 0.98$	q = 0.92
Low Mass Subset	0.145 ± 0.005 $\chi^2/\nu = 1.24$ q = 0.12	0.835 ± 0.015 $\chi^2/\nu = 0.587$ q = 0.98	2.36 ± 0.10 $\chi^2/\nu = 0.13$ $q = 1.0$

Table 5. Mean ICM α_{GAS} Values

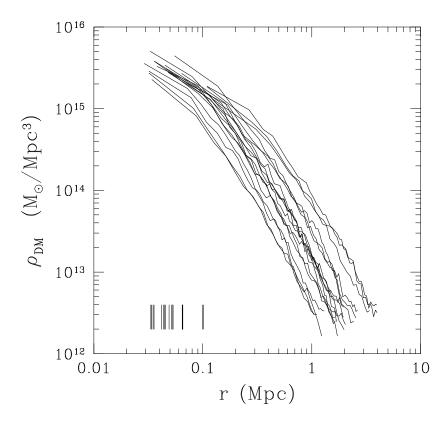
Sample	2F Ensemble	EJ Ensemble
	0.870 ± 0.002 0.860 ± 0.002 0.891 ± 0.002	

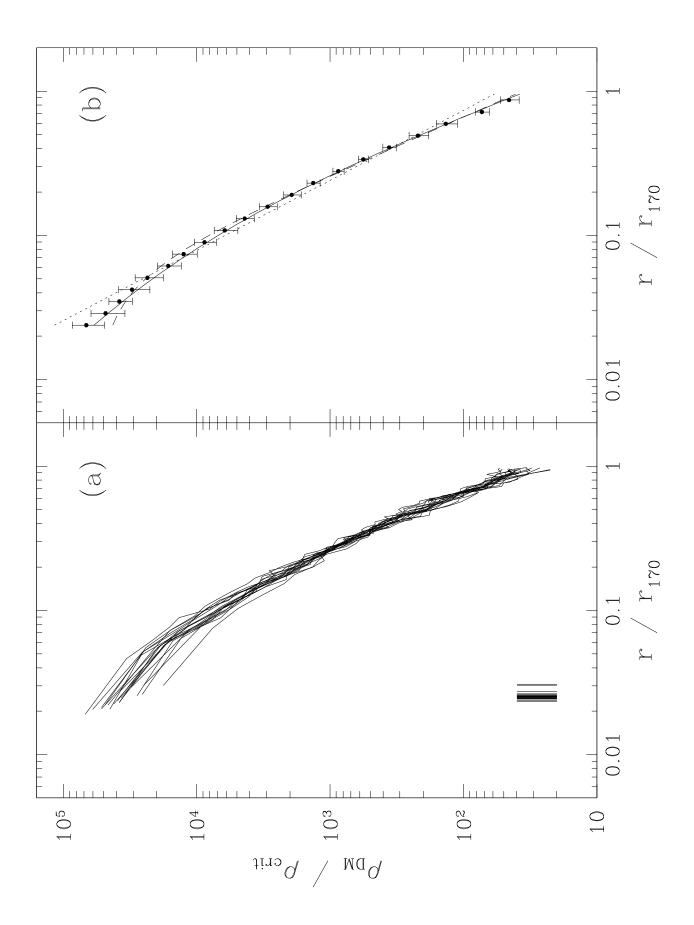
Table 6. Outer Density Profile Slopes

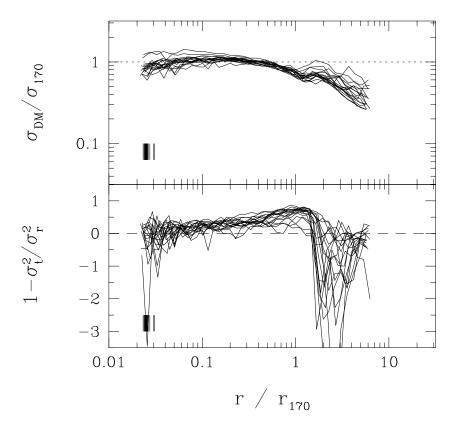
Component	Value
Dark Matter Gas in two-fluid runs Gas in ejection runs Galaxies	-2.39 -2.34 -1.75 $-2.22 to -4.88$

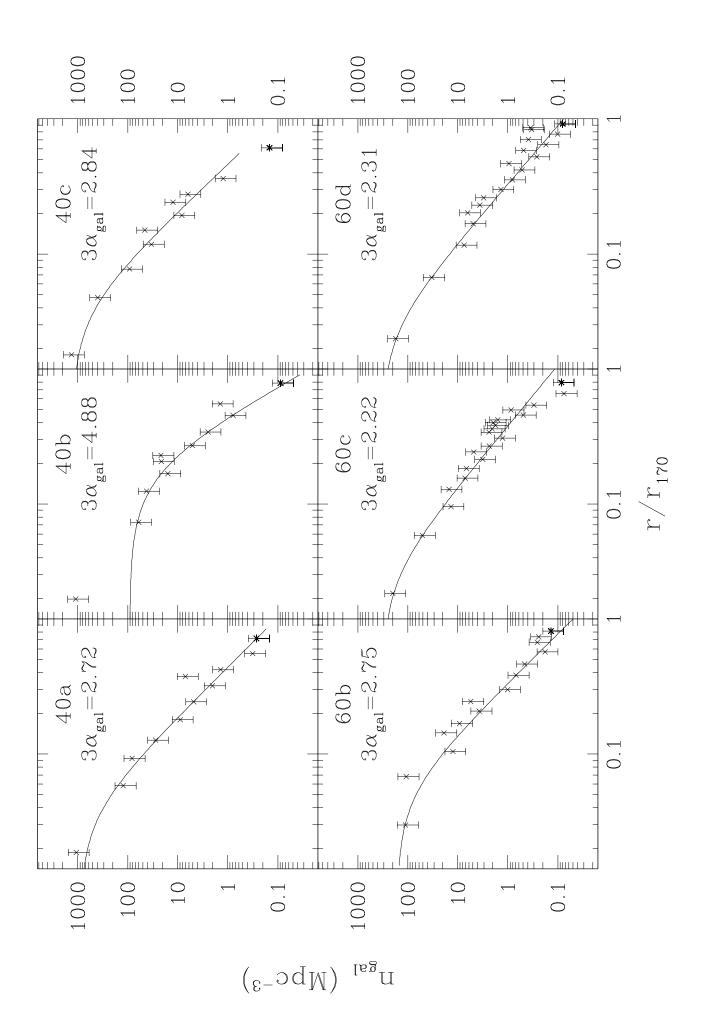


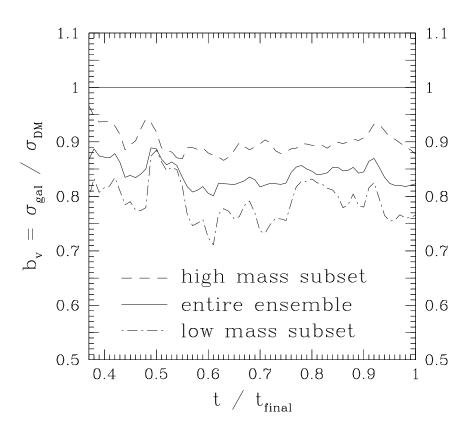
Mean interior density contrast

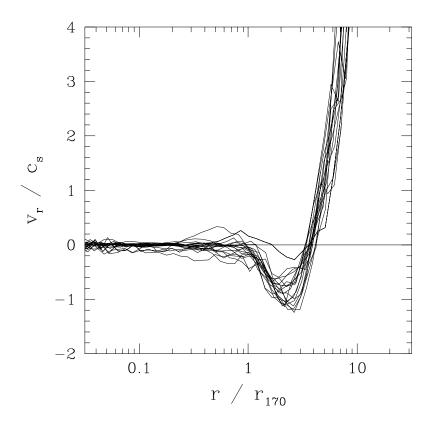


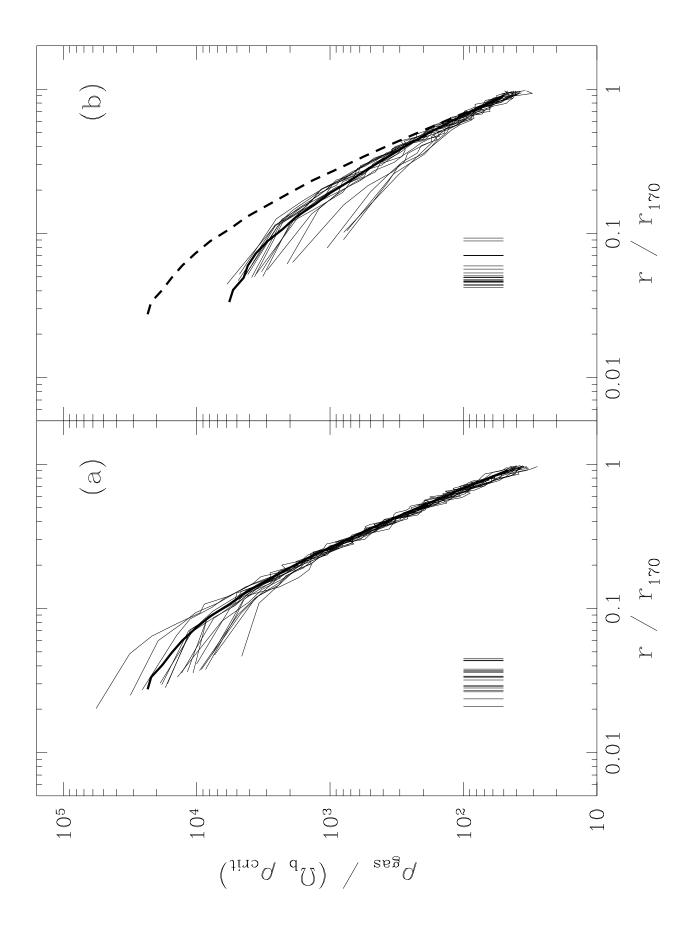


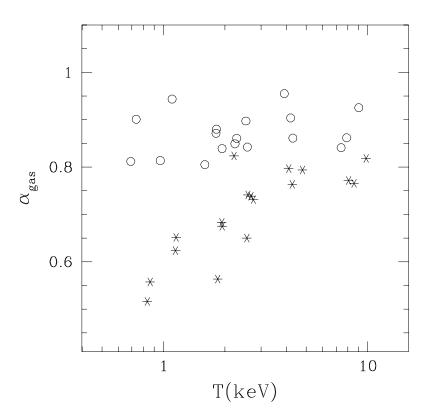


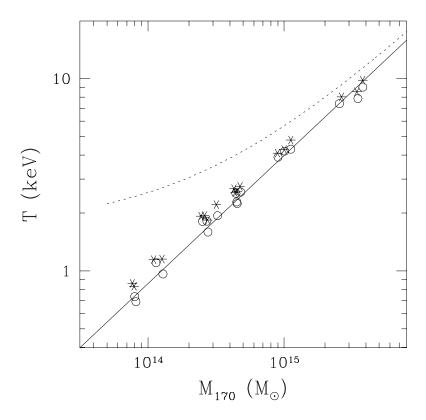


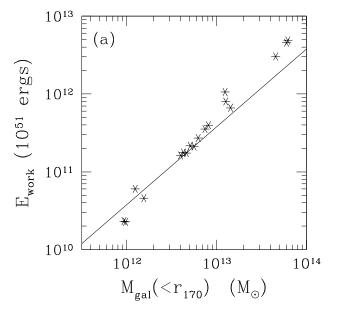


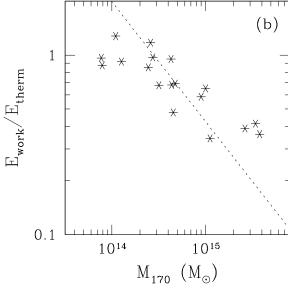


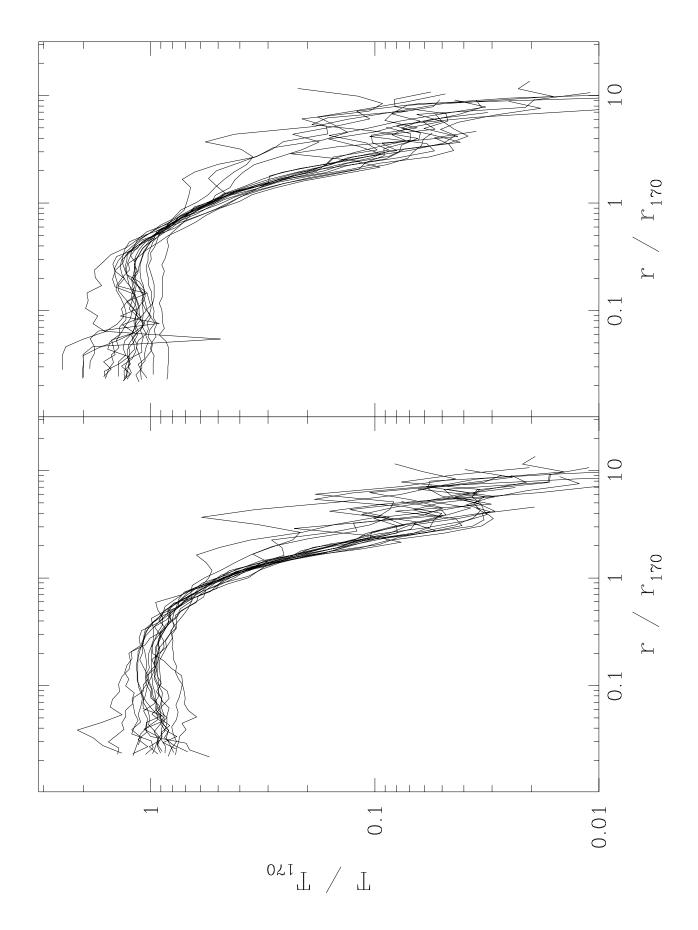


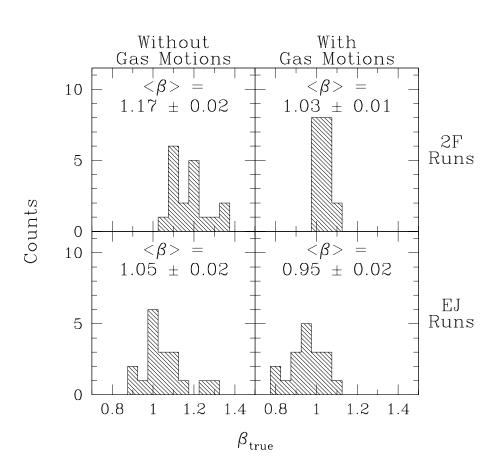


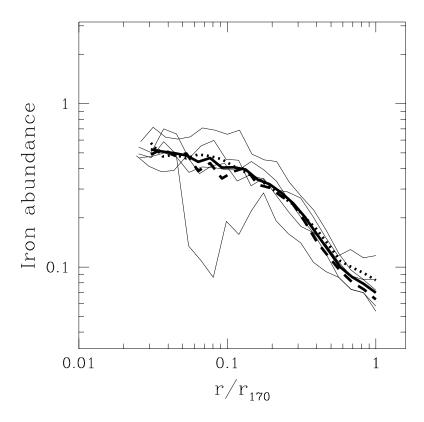


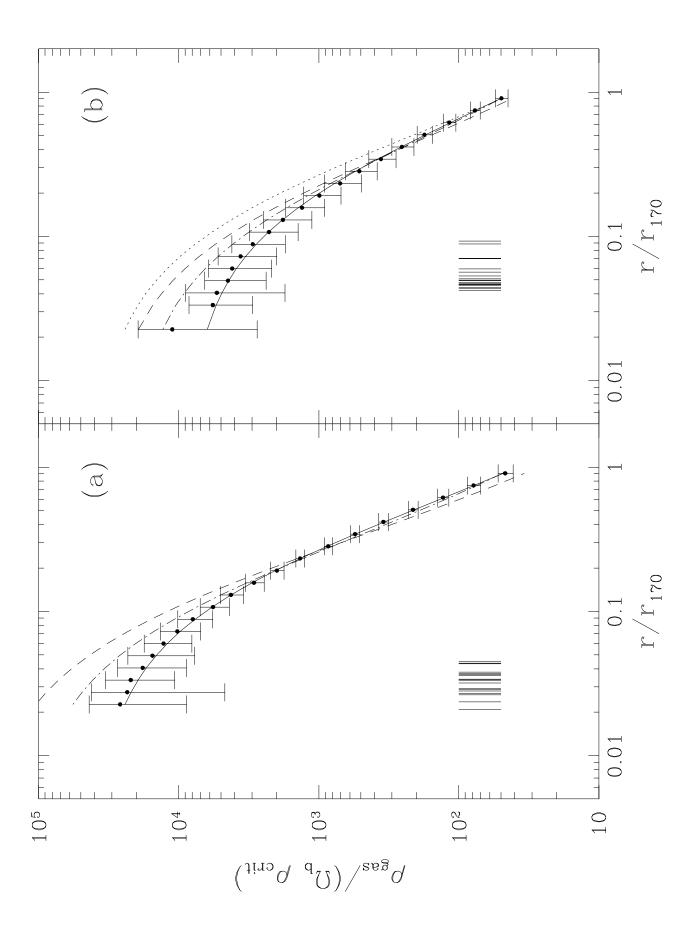


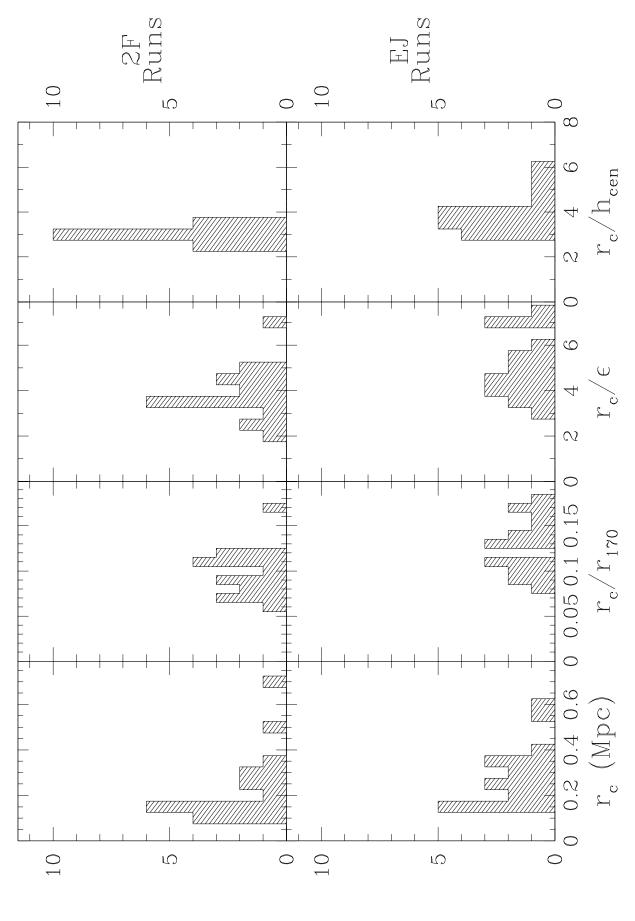












stanos

